

MitoChime: A Machine Learning Pipeline for Detecting PCR-Induced Chimeras in Mitochondrial Illumina Reads

13 by

14 Duranne Duran
15 Yvonne Lin
16 Daniella Pailden

19 January 3, 2026

Abstract

21 Next-generation sequencing (NGS) platforms have advanced research but re-
22 main susceptible to artifacts such as PCR-induced chimeras that compromise
23 mitochondrial genome assembly. These artificial hybrid sequences are prob-
24 lematic for small, circular, and repetitive mitochondrial genomes, where they
25 can generate fragmented contigs and false junctions. Existing detection tools,
26 such as UCHIME, are optimized for amplicon-based microbial community ana-
27 lysis and depend on reference databases or abundance assumptions unsuitable
28 for organellar assembly. To address this gap, this study presents MitoChime,
29 a machine learning pipeline for detecting PCR-induced chimeric reads in *Sar-*
30 *dinella lemuru* Illumina paired-end data without relying on external reference
31 databases.

32 Using simulated datasets containing clean and chimeric reads, a feature
33 set was extracted, combining alignment-based metrics (e.g., supplementary
34 alignments, soft-clipping) with sequence-derived statistics (e.g., k-mer com-
35 position, microhomology). A comparative evaluation of supervised learning
36 models identified tree-based ensembles CatBoost and Gradient Boosting as top
37 performers, achieving an F1-score of 0.77 and an ROC-AUC of 0.84 on held-
38 out test data. Feature importance analysis highlighted soft-clipping and k-mer
39 compositional shifts as the strongest predictors of chimerism, whereas micro-
40 homology contributed minimally. Integrating MitoChime as a pre-assembly
41 step can aid in streamlining mitochondrial reconstruction pipelines.

42 **Keywords:** Chimera detection, Mitochondrial genome,
Assembly, Machine learning

⁴³ **Contents**

⁴⁴	1 Introduction	1
⁴⁵	1.1 Overview	1
⁴⁶	1.2 Problem Statement	3
⁴⁷	1.3 Research Objectives	3
⁴⁸	1.3.1 General Objective	3
⁴⁹	1.3.2 Specific Objectives	4
⁵⁰	1.4 Scope and Limitations of the Research	4
⁵¹	1.5 Significance of the Research	6
⁵²	2 Review of Related Literature	7
⁵³	2.1 The Mitochondrial Genome	7
⁵⁴	2.1.1 Mitochondrial Genome Assembly	8

55	2.2 PCR Amplification and Chimera Formation	9
56	2.3 Existing Traditional Approaches for Chimera Detection	10
57	2.3.1 UCHIME	11
58	2.3.2 UCHIME2	12
59	2.3.3 CATch	13
60	2.3.4 ChimPipe	14
61	2.4 Machine Learning Approaches for Chimera and Sequence Quality	
62	Detection	15
63	2.4.1 Feature-Based Representations of Genomic Sequences . . .	15
64	2.5 Synthesis of Chimera Detection Approaches	16
65	3 Research Methodology	19
66	3.1 Research Activities	19
67	3.1.1 Data Collection	20
68	3.1.2 Feature Extraction Pipeline	23
69	3.1.3 Machine Learning Model Development	26
70	3.1.4 Model Benchmarking, Hyperparameter Optimization, and	
71	Evaluation	27
72	3.1.5 Feature Importance, Feature Selection, and Interpretation	29

73	3.1.6 Validation and Testing	31
74	3.1.7 Documentation	32
75	3.2 Calendar of Activities	32
76	4 Results and Discussion	34
77	4.1 Descriptive Analysis of Features	35
78	4.1.1 Summary Statistics Per Class	35
79	4.1.2 Correlation Analysis of Extracted Features	40
80	4.2 Baseline Classification Performance	41
81	4.3 Effect of Hyperparameter Tuning	43
82	4.4 Detailed Evaluation of Representative Models	44
83	4.4.1 Confusion Matrices and Error Patterns	45
84	4.4.2 ROC and Precision–Recall Curves	46
85	4.5 Feature Importance	47
86	4.5.1 Permutation Importance of Individual Features	47
87	4.5.2 Feature Family Importance	49
88	4.6 Feature Selection	51
89	4.6.1 Cumulative Importance Curve	52

90	4.6.2 Performance Comparison Across Feature Sets	52
91	4.6.3 Interpretation and Final Feature Set Choice	54
92	4.7 Summary of Findings	54
93	A Complete Per-Class Summary Statistics	56
94	B Boxplots for All Numeric Features by Feature Family	60
95	B.0.1 SA Structure (Supplementary Alignment and Segment Met-	
96	rics)	60
97	B.0.2 Clipping-Based Features	62
98	B.0.3 K-mer Features	62
99	B.0.4 Microhomology Features	63
100	B.0.5 Others	63

¹⁰¹ List of Figures

¹⁰²	3.1 Process diagram of the study workflow.	20
¹⁰³	4.1 Boxplots of selected features for clean and chimeric reads.	39
¹⁰⁴	4.2 Feature correlation heatmap showing relationships among alignment-derived and sequence-derived features.	41
¹⁰⁵		
¹⁰⁶	4.3 Test F1 of all baseline classifiers, showing that no single model clearly dominates and several achieve comparable performance. . .	42
¹⁰⁷		
¹⁰⁸	4.4 Comparison of test F1 (left) and ROC–AUC (right) for baseline	
¹⁰⁹	and tuned models.	44
¹¹⁰		
¹¹¹	4.5 Confusion matrices for the four representative models on the held-out test set.	46
¹¹²		
¹¹³	4.6 ROC (left) and precision–recall (right) curves for the four representative models on the held-out test set.	47
¹¹⁴		
¹¹⁵	4.7 Permutation-based feature importance for four representative classifiers.	49

116	4.8 Aggregated feature family importance across four models.	51
117	4.9 Cumulative importance curve of features sorted by importance. .	52
118	4.10 Comparison of F1 and ROC–AUC for the full, top-4 selected, and	
119	no-microhomology feature set variants.	53
120	B.1 Boxplots of SA Structure features by class (1/2).	60
121	B.2 Boxplots of SA Structure features by class (2/2).	61
122	B.3 Boxplots of clipping-based features by class.	62
123	B.4 Boxplots of k-mer features by class.	62
124	B.5 Boxplots of microhomology features by class.	63
125	B.6 Boxplots of other numeric features by class.	63

126 List of Tables

¹³⁵ Chapter 1

¹³⁶ Introduction

¹³⁷ 1.1 Overview

¹³⁸ The rapid advancement of next-generation sequencing (NGS) technologies has
¹³⁹ transformed genomic research by enabling high-throughput and cost-effective
¹⁴⁰ DNA analysis (Metzker, 2010). Among current platforms, Illumina sequencing
¹⁴¹ remains the most widely adopted, capable of producing millions of short reads
¹⁴² that can be assembled into reference genomes or analyzed for genetic variation
¹⁴³ (Bentley et al., 2008; Glenn, 2011). Despite its high base-calling accuracy,
¹⁴⁴ Illumina sequencing is prone to artifacts introduced during library preparation,
¹⁴⁵ particularly polymerase chain reaction (PCR)-induced chimeras, which are ar-
¹⁴⁶ tificial hybrid sequences that do not exist in the true genome (Judo, Wedel, &
¹⁴⁷ Wilson, 1998).

¹⁴⁸ PCR chimeras form when incomplete extension products from one template

anneal to an unrelated DNA fragment and are extended, creating recombinant reads (Qiu et al., 2001). In mitochondrial genome assembly, such artifacts are especially problematic because the mitochondrial genome is small, circular, and often repetitive (Boore, 1999; Cameron, 2014). Even a small number of chimeric or misjoined reads can reduce assembly contiguity and introduce false junctions during organelle genome reconstruction (Dierckxsens, Mardulyn, & Smits, 2017; Hahn, Bachmann, & Chevreux, 2013; Jin et al., 2020). Existing assembly tools such as GetOrganelle and MITObim assume that input reads are largely free of such artifacts (Hahn et al., 2013; Jin et al., 2020). Consequently, undetected chimeras may produce fragmented assemblies or misidentified organellar boundaries. To ensure accurate reconstruction of mitochondrial genomes, a reliable method for detecting PCR-induced chimeras before assembly is essential.

This study focuses on mitochondrial sequencing data from the genus *Sardinella*, a group of small pelagic fishes widely distributed in Philippine waters. Among them, *Sardinella lemuru* (Bali sardinella) is one of the country's most abundant and economically important species, providing protein and livelihood to coastal communities (Labrador, Agmata, Palermo, Ravago-Gotanco, & Pante, 2021; Willette, Bognot, Mutia, & Santos, 2011). Accurate mitochondrial assemblies are critical for understanding its population genetics, stock structure, and evolutionary history. However, assembly pipelines often encounter errors or fail to complete due to undetected chimeric reads. To address this gap, this research introduces MitoChime, a machine learning pipeline designed to detect PCR-induced chimeric reads using both alignment-based and sequence-derived statistical features. The tool aims to provide bioinformatics laboratories, particularly the Philippine Genome Center Visayas (PGC Visayas), with an efficient

174 solution for improving mitochondrial genome reconstruction.

175 1.2 Problem Statement

176 Chimeric reads can distort assembly graphs and cause misassemblies, with par-
177 ticularly severe effects in mitochondrial genomes (Boore, 1999; Cameron, 2014).
178 Existing assembly pipelines such as GetOrganelle, MITObim, and NOVOPlasty
179 assume that sequencing reads are free of such artifacts (Dierckxsens et al., 2017;
180 Hahn et al., 2013; Jin et al., 2020). At PGC Visayas, several mitochondrial as-
181 semblies have failed or yielded incomplete contigs despite sufficient coverage, sug-
182 gesting that undetected chimeric reads compromise assembly reliability. Mean-
183 while, existing chimera detection tools such as UCHIME and VSEARCH were
184 developed primarily for amplicon-based community analysis and rely heavily on
185 reference or taxonomic comparisons (Edgar, Haas, Clemente, Quince, & Knight,
186 2011; Rognes, Flouri, Nichols, Quince, & Mahé, 2016). These approaches are un-
187 suitable for single-species organellar data, where complete reference genomes are
188 often unavailable.

189 1.3 Research Objectives

190 1.3.1 General Objective

191 This study aims to develop and evaluate a machine learning-based pipeline (Mi-
192 toChime) that detects PCR-induced chimeric reads in *Sardinella lemuru* mito-

₁₉₃ chondrial sequencing data in order to improve the quality and reliability of down-
₁₉₄ stream mitochondrial genome assemblies.

₁₉₅ 1.3.2 Specific Objectives

₁₉₆ Specifically, the study aims to:

- ₁₉₇ 1. construct simulated *Sardinella lemuru* Illumina paired-end datasets contain-
₁₉₈ ing both clean and PCR-induced chimeric reads,
- ₁₉₉ 2. extract alignment-based and sequence-based features such as k-mer compo-
₂₀₀ sition, junction complexity, and split-alignment counts from both clean and
₂₀₁ chimeric reads,
- ₂₀₂ 3. train, validate, and compare supervised machine learning models for classi-
₂₀₃ fying reads as clean or chimeric,
- ₂₀₄ 4. determine feature importance and identify indicators of PCR-induced
₂₀₅ chimerism,
- ₂₀₆ 5. integrate the optimized classifier into a modular and interpretable pipeline
₂₀₇ deployable on standard computing environments at PGC Visayas.

₂₀₈ 1.4 Scope and Limitations of the Research

₂₀₉ This study focuses solely on PCR-induced chimeric reads in *Sardinella lemuru*
₂₁₀ mitochondrial sequencing data, with the species choice guided by four consid-
₂₁₁ erations: (1) to limit interspecific variation in mitochondrial genome size, GC

212 content, and repetitive regions so that differences in read patterns can be at-
213 tributed more directly to PCR-induced chimerism, (2) to align the analysis with
214 relevant *S. lemuru* sequencing projects at PGC Visayas, (3) to take advantage of
215 the availability of *S. lemuru* mitochondrial assemblies and raw datasets in public
216 repositories such as the National Center for Biotechnology Information (NCBI),
217 which facilitates reference selection and benchmarking, and (4) to develop a tool
218 that directly supports local studies on *S. lemuru* population structure and fisheries
219 management.

220 The study emphasizes `wgsim`-based simulations and selected empirical mito-
221 chondrial datasets from *S. lemuru*. It excludes naturally occurring chimeras, nu-
222 clear mitochondrial pseudogenes (NUMTs), and large-scale assembly rearrange-
223 ments in nuclear genomes. Feature extraction is restricted to low-dimensional
224 alignment and sequence statistics, such as k-mer frequency profiles, GC con-
225 tent, soft and hard clipping metrics, and split-alignment counts rather than high-
226 dimensional deep learning embeddings. This design keeps model behaviour inter-
227 pretable and ensures that the pipeline can be run on standard workstations at
228 PGC Visayas. Testing on long-read platforms (e.g., Nanopore, PacBio) and other
229 taxa is outside the scope of this project.

230 Other limitations in this study include the following: simulations with vary-
231 ing error rates were not performed, so the effect of different sequencing errors on
232 model performance remains unexplored; alternative parameter settings, including
233 k-mer lengths and microhomology window sizes, were not systematically tested,
234 which could affect the sensitivity of both k-mer and microhomology feature de-
235 tection; and the machine learning models rely on supervised training with labeled
236 examples, which may limit their ability to detect novel or unexpected chimeric

²³⁷ patterns.

²³⁸ 1.5 Significance of the Research

²³⁹ This research provides both methodological and practical contributions to mito-
²⁴⁰ chondrial genomics and bioinformatics. First, MitoChime detects PCR-induced
²⁴¹ chimeric reads prior to genome assembly, with the goal of improving the con-
²⁴² tiguity and correctness of *Sardinella lemuru* mitochondrial assemblies. Second,
²⁴³ it replaces informal manual curation with a documented workflow, improving au-
²⁴⁴ tomation and reproducibility. Third, the pipeline is designed to run on computing
²⁴⁵ infrastructures commonly available in regional laboratories, enabling routine use
²⁴⁶ at facilities such as PGC Visayas. Finally, more reliable mitochondrial assemblies
²⁴⁷ for *S. lemuru* provide a stronger basis for downstream applications in the field of
²⁴⁸ fisheries and genomics.

²⁴⁹ **Chapter 2**

²⁵⁰ **Review of Related Literature**

²⁵¹ This chapter presents an overview of the literature relevant to the study. It
²⁵² discusses the biological and computational foundations underlying mitochondrial
²⁵³ genome analysis and assembly, as well as existing tools, algorithms, and techniques
²⁵⁴ related to chimera detection and genome quality assessment. The chapter aims to
²⁵⁵ highlight the strengths, limitations, and research gaps in current approaches that
²⁵⁶ motivate the development of the present study.

²⁵⁷ **2.1 The Mitochondrial Genome**

²⁵⁸ Mitochondrial genome (mtDNA) is a small, typically circular molecule found in
²⁵⁹ most eukaryotes. It encodes essential genes involved in oxidative phosphorylation
²⁶⁰ and energy metabolism. Because of its conserved structure, mtDNA has become
²⁶¹ a valuable genetic marker for studies in population genetics and phylogenetics
²⁶² (Anderson et al., 1981; Boore, 1999). In animal species, the mitochondrial genome

ranges from 15–20 kilobase and contains 13 protein-coding genes, 22 tRNAs, and two rRNAs arranged compactly without introns (Gray, 2012). In comparison to nuclear DNA, the ratio of the number of copies of mtDNA is higher and has simple organization which make it particularly suitable for genome sequencing and assembly studies (Dierckxsens et al., 2017).

2.1.1 Mitochondrial Genome Assembly

Mitochondrial genome assembly refers to the reconstruction of the complete mitochondrial DNA (mtDNA) sequence from raw or fragmented sequencing reads. It is conducted to obtain high-quality, continuous representations of the mitochondrial genome that can be used for a wide range of analyses, including species identification, phylogenetic reconstruction, evolutionary studies, and investigations of mitochondrial diseases. Because mtDNA evolves rapidly, its assembled sequence provides valuable insights into population structure, lineage divergence, and adaptive evolution across taxa (Boore, 1999). Compared to nuclear genome assembly, assembling the mitochondrial genome is often considered more straightforward but still encounters technical challenges such as the formation of chimeric reads. Commonly used tools for mitogenome assembly such as GetOrganelle and MITObim operate under the assumption of organelle genome circularity, and are vulnerable when chimeric reads disrupt this circular structure, resulting in assembly errors (Hahn et al., 2013; Jin et al., 2020).

283 2.2 PCR Amplification and Chimera Formation

284 PCR plays an important role in NGS library preparation, as it amplifies target
285 DNA fragments for downstream analysis. However as previously mentioned, the
286 amplification process can also introduce chimeric reads which compromises the
287 quality of the input reads supplied to sequencing or assembly workflows. Chimeras
288 typically arise when incomplete extension occurs during a PCR cycle. This causes
289 the DNA polymerase to switch from one template to another and generate hy-
290 brid recombinant molecules (Judo et al., 1998). Artificial chimeras are produced
291 through such amplification errors, whereas biological chimeras occur naturally
292 through genomic rearrangements or transcriptional events.

293 In the context of amplicon-based sequencing, the presence of chimeras can in-
294 flate estimates of genetic or microbial diversity and may cause misassemblies dur-
295 ing genome reconstruction. Qin et al. (2023) has reported that chimeric sequences
296 may account for more than 10% of raw reads in amplicon datasets. This artifact
297 tends to be most prominent among rare operational taxonomic units (OTUs) or
298 singletons, which are sometimes misinterpreted as novel diversity, further caus-
299 ing the complication of microbial diversity analyses (Gonzalez, Zimmermann, &
300 Saiz-Jimenez, 2004). As such, determining and minimizing PCR-induced chimera
301 formation is vital for improving the quality of mitochondrial genome assemblies,
302 and ensuring the reliability of amplicon sequencing data.

303 **2.3 Existing Traditional Approaches for Chimera**

304 **Detection**

305 Several computational tools have been developed to identify chimeric sequences in
306 NGS datasets. These tools generally fall into two categories: reference-based and
307 de novo approaches. Reference-based chimera detection, also known as database-
308 dependent detection, is one of the earliest and most widely used computational
309 strategies for identifying chimeric sequences in amplicon-based community studies.
310 These methods rely on the comparison of each query sequence against a curated,
311 high-quality database of known, non-chimeric reference sequences (Edgar et al.,
312 2011).

313 On the other hand, the de novo chimera detection, also referred to as reference-
314 free detection, represents an alternative computational paradigm that identifies
315 chimeric sequences without reliance on external reference databases. This method
316 infer chimeras based on internal relationships among the sequences present within
317 the dataset itself, making it particularly advantageous in studies of under explored
318 or taxonomically diverse communities where comprehensive reference databases
319 are unavailable or incomplete (Edgar, 2016; Edgar et al., 2011). The underlying
320 assumption on this method is that during PCR, true biological sequences are
321 generally more abundant as they are amplified early and dominate the read pool,
322 whereas chimeric sequences appear later and are generally less abundant. The
323 de novo approach leverage this abundance hierarchy, treating the most abundant
324 sequences as supposed parents and testing whether less abundant sequences can
325 be reconstructed as mosaics of these templates. Compositional and structural
326 similarity are also evaluated to check whether different regions of a candidate

327 sequence correspond to distinct high-abundance sequences.

328 In practice, many modern bioinformatics pipelines combine both paradigms
329 sequentially: an initial de novo step identifies dataset-specific chimeras, followed
330 by a reference-based pass that removes remaining artifacts relative to established
331 databases (Edgar, 2016). These two methods of detection form the foundation of
332 tools such as UCHIME and later UCHIME2.

333 2.3.1 UCHIME

334 UCHIME is one of the most widely used tools for detecting chimeric sequences in
335 amplicon-based studies and remains a standard quality-control step in microbial
336 community analysis. Its core strategy is to test whether a query sequence (Q) can
337 be explained as a mosaic of two parent sequences, (A and B), and to score this
338 relationship using a structured alignment model (Edgar et al., 2011).

339 In reference mode, UCHIME divides the query into several segments and maps
340 them against a curated database of non-chimeric sequences. Candidate parents
341 are identified, and a three-way alignment is constructed. The algorithm assigns
342 “Yes” votes when different segments of the query match different parents and
343 “No” votes when the alignment contradicts a chimeric pattern. The final score
344 reflects the balance of these votes. In de novo mode, UCHIME operationalizes the
345 abundance-skew principle described earlier: high-abundance sequences are treated
346 as candidate parents, and lower-abundance sequences are evaluated as potential
347 mosaics. This makes the method especially useful when no reliable reference
348 database exists.

349 Although UCHIME is highly sensitive, it faces key constraints. Chimeras
350 formed from parents with very low divergence (below 0.8%) are difficult to detect
351 because they are nearly indistinguishable from sequencing errors. Accuracy in ref-
352 erence mode depends strongly on database completeness, while de novo detection
353 assumes that true parents are both present and sufficiently more abundant, such
354 conditions are not always met.

355 **2.3.2 UCHIME2**

356 UCHIME2 extends the original algorithm with refinements tailored for high-
357 resolution sequencing data. One of its major contributions is a re-evaluation
358 of benchmarking practices. Edgar (2016) demonstrated that earlier accuracy es-
359 timates for chimera detection were overly optimistic because they relied on un-
360 realistic scenarios where all true parent sequences were assumed to be present.
361 Using the more rigorous CHSIMA benchmark, UCHIME2 showed the prevalence
362 of “fake models” or real biological sequences that can be perfectly reconstructed
363 as apparent chimeras of other sequences, which suggests that perfect chimera de-
364 tection is theoretically unattainable. UCHIME2 also introduces several preset
365 modes (e.g., denoised, balanced, sensitive, specific, high-confidence) designed to
366 tune sensitivity and specificity depending on dataset characteristics. These modes
367 allow users to adjust the algorithm to the expected noise level or analytical goals.

368 Despite these improvements, UCHIME2 must be applied with caution. The
369 website manual explicitly advises against using UCHIME2 as a standalone
370 chimera-filtering step in OTU clustering or denoising workflows because doing so
371 can inflate both false positives and false negatives (Edgar, n.d.).

372 2.3.3 CATch

373 As previously mentioned, UCHIME (Edgar et al., 2011) relied on alignment-based
374 sequences in amplicon data. However, researchers soon observed that different al-
375 gorithms often produced inconsistent predictions. A sequence might be identified
376 as chimeric by one tool but classified as non-chimeric by another, resulting in
377 unreliable filtering outcomes across studies.

378 To address these inconsistencies, Mysara, Saeys, Leys, Raes, and Monsieurs
379 (2015) developed the Classifier for Amplicon Tool Chimeras (CATCh), which rep-
380 resents the first ensemble machine learning system designed for chimera detection
381 in 16S rRNA amplicon sequencing. Rather than depending on a single detec-
382 tion strategy, CATCh integrates the outputs of several established tools, includ-
383 ing UCHIME, ChimeraSlayer, DECIPHER, Pintail, and Perseus. The individual
384 scores and binary decisions generated by these tools are used as input features for
385 a supervised learning model. The algorithm employs a Support Vector Machine
386 (SVM) with a Pearson VII Universal Kernel (PUK) to determine optimal weight-
387 ings among the input features and to assign each sequence a probability of being
388 chimeric.

389 Benchmarking in both reference-based and de novo modes demonstrated signif-
390 icant performance improvements. CATCh achieved sensitivities of approximately
391 85 percent in reference-based mode and 92 percent in de novo mode, with corre-
392 sponding specificities of approximately 96 percent and 95 percent. These results
393 indicate that CATCh detected 7 to 12 percent more chimeras than any individual
394 algorithm while maintaining high precision.

395 **2.3.4 ChimPipe**

396 Among the available tools for chimera detection, ChimPipe is a pipeline developed
397 to identify chimeric sequences such as biological chimeras. It uses both discordant
398 paired-end reads and split-read alignments to improve the accuracy and sensitivity
399 of detecting biological chimeras (Rodriguez-Martin et al., 2017). By combining
400 these two sources of information, ChimPipe achieves better precision than meth-
401 ods that depend on a single type of indicator.

402 The pipeline works with many eukaryotic species that have available genome
403 and annotation data (Rodriguez-Martin et al., 2017). It can also predict multiple
404 isoforms for each gene pair and identify breakpoint coordinates that are useful
405 for reconstructing and verifying chimeric transcripts. Tests using both simulated
406 and real datasets have shown that ChimPipe maintains high accuracy and reliable
407 performance.

408 ChimPipe lets users adjust parameters to fit different sequencing protocols or
409 organism characteristics. Experimental results have confirmed that many chimeric
410 transcripts detected by the tool correspond to functional fusion proteins, demon-
411 strating its utility for understanding chimera biology and its potential applications
412 in disease research (Rodriguez-Martin et al., 2017).

413 **2.4 Machine Learning Approaches for Chimera**

414 **and Sequence Quality Detection**

415 Traditional chimera detection tools rely primarily on heuristic or alignment-based
416 rules. Recent advances in machine learning (ML) have demonstrated that models
417 trained on sequence-derived features can effectively capture compositional and
418 structural patterns in biological sequences. Although most existing ML systems
419 such as those used for antibiotic resistance prediction, taxonomic classification,
420 or viral identification are not specifically designed for chimera detection, they
421 highlight how data-driven models can outperform similarity-based heuristics by
422 learning intrinsic sequence signatures. In principle, ML frameworks can integrate
423 indicators such as k-mer frequencies, GC-content variation and split-alignment
424 metrics to identify subtle anomalies that may indicate a chimeric origin (Arango
425 et al., 2018; Liang, Bible, Liu, Zou, & Wei, 2020; Ren et al., 2020).

426 **2.4.1 Feature-Based Representations of Genomic Se-**

427 **quences**

428 Feature extraction converts DNA sequences into numerical representations suit-
429 able for machine learning models. One approach is k-mer frequency analysis,
430 which counts short nucleotide sequences within a read (Vervier, Mahé, Tournoud,
431 Veyrieras, & Vert, 2015). High-frequency k-mers, including simple repeats such
432 as “AAAAAA,” can highlight repetitive or unusual regions that may occur near
433 chimeric junctions. Comparing k-mer patterns across adjacent parts of a read can
434 help identify such regions, while GC content provides an additional descriptor of

435 local sequence composition (Ren et al., 2020).

436 Alignment-derived features further inform junction detection. Long-read tools
437 such as Sniffles (Sedlazeck et al., 2018) use split alignments to locate breakpoints
438 across extended sequences, whereas short-read aligners like Minimap2 (Li, 2018)
439 report supplementary and secondary alignments that indicate local discontinu-
440 ities. Split alignments, where parts of a read map to different regions, can reveal
441 template-switching events. These features complement k-mer profiles and en-
442 hance detection of potentially chimeric reads, even in datasets with incomplete
443 references.

444 Microhomology, or short sequences shared between adjacent segments, is an-
445 other biologically meaningful feature. Short microhomologies, typically 3–20 bp,
446 are involved in template switching both in cellular repair pathways and during
447 PCR, where they act as signatures of chimera formation (Peccoud et al., 2018;
448 Sfeir & Symington, 2015). In PCR-induced chimeras, short identical sequences
449 at junctions provide a clear signature of chimerism. Measuring the longest exact
450 overlap at each breakpoint complements k-mer and alignment features and helps
451 identify reads that are potentially chimeric.

452 2.5 Synthesis of Chimera Detection Approaches

453 To provide an integrated overview of the literature discussed in this chapter, Ta-
454 ble 2.1 summarizes the major chimera detection studies, their methodological
455 approaches, and their known limitations.

Table 2.1: Comparison of Chimera Detection Approaches and Tools

Method / Tool	Core Approach	Key Limitations
Reference-based Detection	Compares each query sequence against curated databases of verified, non-chimeric sequences; evaluates segment similarity to identify mosaic patterns.	Accuracy depends on database completeness; performs poorly for novel taxa or missing parents; limited sensitivity for low-divergence chimeras.
De novo Detection	Identifies chimeras using only internal dataset structure; leverages abundance hierarchy and compositional similarity to infer whether low-abundance sequences can be reconstructed from abundant parents.	Assumes true sequences are more abundant; fails when amplification bias distorts abundances; struggles when parental sequences are similarly abundant or highly similar.
UCHIME	Alignment-based model that partitions the query into segments, identifies parent candidates, and computes a chimera score via a three-way alignment; supports reference and de novo modes.	Reduced accuracy for very closely related parents (<0.8% divergence); sensitive to incomplete databases; de novo mode fails if parents are absent or not sufficiently more abundant.
UCHIME2	Updated UCHIME with improved benchmarking (CHSIMA) and multiple sensitivity/specificity presets; better handles incomplete references and dataset variability.	“Fake models” limit theoretical accuracy; genuine variants may mimic chimeras; not recommended as a standalone step in OTU or denoising pipelines due to increased false positives/negatives.
CATCh	First ensemble ML model for 16S chimera detection; integrates outputs of UCHIME, ChimeraSlayer, DECIPHER, Pintail, and Perseus using an SVM to boost overall prediction accuracy.	Performance constrained by underlying tools; ML model cannot capture features not present in component algorithms; may misclassify in highly novel or low-coverage datasets.
ChimPipe	Pipeline for detecting biological chimeras in RNA-seq using discordant paired-end reads and split-read alignments; identifies isoforms and breakpoint coordinates.	Requires high-quality genome and annotation; tailored to RNA-seq rather than amplicons; computationally intensive; limited to organisms with available reference genomes.

456 Across existing studies, no single approach reliably detects all forms of chimeric
457 sequences, and the reviewed literature consistently shows that chimeras remain a
458 persistent challenge in genomics and bioinformatics. Although the surveyed tools
459 are not designed specifically for organelle genome assembly, they provide valua-
460 able insights into which methodological strategies are effective and where current
461 approaches fall short. These limitations collectively define a clear research gap:
462 the need for a specialized, feature-driven detection framework tailored to PCR-
463 induced mitochondrial chimeras. Addressing this gap aligns with the research
464 objective outlined in Section 1.3, which is to develop and evaluate a machine
465 learning-based pipeline (MitoChime) that improves the quality of downstream
466 mitochondrial genome assembly. In support of this aim, the subsequent chapters
467 describe the design, implementation, and evaluation of the proposed tool.

⁴⁶⁸ Chapter 3

⁴⁶⁹ Research Methodology

⁴⁷⁰ This chapter outlines the steps involved in completing the study, including data
⁴⁷¹ gathering, generating simulated mitochondrial Illumina reads, preprocessing and
⁴⁷² indexing the data, developing a feature extraction pipeline to obtain read-level fea-
⁴⁷³ tures, applying machine learning algorithms for chimera detection, implementing
⁴⁷⁴ feature selection methods, and validating and comparing model performance.

⁴⁷⁵ 3.1 Research Activities

⁴⁷⁶ As illustrated in Figure 3.1, this study carried out a sequence of procedures to
⁴⁷⁷ detect PCR-induced chimeric reads in mitochondrial genomes. The process began
⁴⁷⁸ with collecting a mitochondrial reference sequence of *Sardinella lemuru* from the
⁴⁷⁹ National Center for Biotechnology Information (NCBI) database, which was used
⁴⁸⁰ as a reference for generating simulated clean and chimeric reads. These reads
⁴⁸¹ were subsequently indexed and mapped. The resulting collections then passed

482 through a feature extraction pipeline that computed k-mer profiles, supplementary
483 alignment (SA) features, and microhomology information to prepare the data
484 for model construction. The machine learning models were trained using the
485 processed input, evaluated using cross-validation and held-out testing, tuned for
486 improved performance, and then subjected to feature importance and feature
487 selection analyses before final validation.

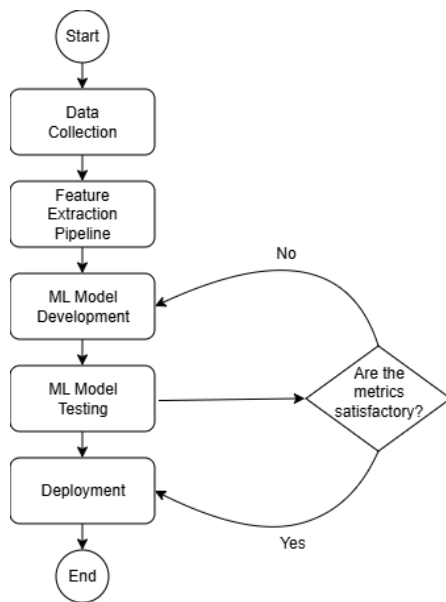


Figure 3.1: Process diagram of the study workflow.

488 3.1.1 Data Collection

489 The mitochondrial genome reference sequence of *S. lemuru* was obtained from the
490 NCBI database (accession number NC_039553.1) in FASTA format and was used
491 to generate simulated reads.

492 This step was scheduled to begin in the first week of November 2025 and
493 expected to be completed by the end of that week, with a total duration of ap-

494 proximately one (1) week.

495 Data Preprocessing

496 All steps in the simulation and preprocessing pipeline were executed using a cus-
497 tom script in Python (Version 3.11). The script runs each stage, including read
498 simulation, reference indexing, mapping, and alignment processing, in a fixed se-
499 quence.

500 `wgsim` (Version 1.13) was used to simulate 10,000 paired-end fragments, pro-
501 ducing 20,000 reads (10,000 forward and 10,000 reverse) from the original refer-
502 ence (`original_reference.fasta`) and designated as clean reads. The tool was
503 selected because it provides fast generation of Illumina-like reads with controllable
504 error rates, using the following command:

```
505 wgsim -1 150 -2 150 -r 0 -R 0 -X 0 -e 0.05 -N 10000 \  
506           original_reference.fasta ref1.fastq ref2.fastq
```

507 Chimeric sequences were then generated from the same reference FASTA
508 file using a separate Python script. Two non-adjacent segments were ran-
509 domly selected such that their midpoint distances fell within specified minimum
510 and maximum thresholds. The script attempted to retain microhomology to
511 mimic PCR-induced template switching. The resulting chimeras were written
512 to `chimera_reference.fasta` and processed with `wgsim` to simulate 10,000
513 paired-end fragments, generating 20,000 chimeric reads (10,000 forward reads in
514 `chimeric1.fastq` and 10,000 reverse reads in `chimeric2.fastq`) using the same
515 command format as above.

516 Next, a `minimap2` index of the reference genome was created using:

```
517  minimap2 -d ref.mmi original_reference.fasta
```

518 Minimap2 (Version 2.28) was used to map simulated clean and chimeric reads
519 to the original reference. An index (`ref.mmi`) was first generated to enable efficient
520 alignment, and mapping produced the alignment features used as input for the
521 machine learning model. The reads were mapped using the following commands:

```
522  minimap2 -ax sr -t 8 ref.mmi ref1.fastq ref2.fastq > clean.sam
```

```
523  minimap2 -ax sr -t 8 ref.mmi \  
524        chimeric1.fastq chimeric2.fastq > chimeric.sam
```

525 The resulting clean and chimeric SAM files contain the alignment positions of
526 each read relative to the original reference genome. These files were then converted
527 to BAM format, sorted, and indexed using `samtools` (Version 1.20):

```
528  samtools view -bS clean.sam -o clean.bam  
529  samtools view -bS chimeric.sam -o chimeric.bam  
530  
531  samtools sort clean.bam -o clean.sorted.bam  
532  samtools index clean.sorted.bam  
533  
534  samtools sort chimeric.bam -o chimeric.sorted.bam  
535  samtools index chimeric.sorted.bam
```

536 The total number of simulated reads was expected to be 40,000. The final col-
537 lection of reads contained 19,984 clean reads and 20,000 chimeric reads (39,984 en-
538 tries in total), providing a roughly balanced distribution between the two classes.
539 After alignment with `minimap2`, only 19,984 clean reads remained because un-
540 mapped reads were not included in the BAM file. Some sequences failed to align
541 due to the error rate defined during `wgsim` simulation, which produced mismatches
542 that caused certain reads to fall below the aligner's matching threshold.

543 This whole process was scheduled to start in the second week of November 2025
544 and was expected to be completed by the last week of November 2025, with a total
545 duration of approximately three (3) weeks.

546 **3.1.2 Feature Extraction Pipeline**

547 This stage directly followed the alignment phase, utilizing the resulting BAM files
548 (specifically `chimeric.sorted.bam` and `clean.sorted.bam`). A custom Python
549 script was created to efficiently process each primary-mapped read to extract
550 the necessary set of features, which were then compiled into a structured feature
551 matrix in TSV format. The pipeline's core functionality relied on the `Pysam`
552 (Version 0.22) library for parsing BAM structures and `NumPy` (Version 1.26) for
553 array operations and computations. To ensure correctness and adherence to best
554 practices, bioinformatics experts at PGC Visayas were consulted to validate the
555 pipeline design, feature extraction logic, and overall data integrity.

556 This stage of the study was scheduled to begin in the last week of Novem-
557 ber 2025 and conclude by the first week of December 2025, with an estimated

558 total duration of approximately two (2) weeks.

559 The pipeline focused on three feature families that collectively capture bi-
560 ological signatures associated with PCR-induced chimeras: (1) supplementary
561 alignment (SA) and alignment-structure metrics, (2) k-mer composition differ-
562 ence, and (3) microhomology around putative junctions. Additional alignment
563 quality indicators such as mapping quality were also included.

564 **Supplementary Alignment and Alignment-Structure Features**

565 Split-alignment information was derived from the SA tag embedded in each pri-
566 mary read of the BAM file. This tag is typically associated with reads that map to
567 multiple genomic locations, suggesting a chimeric structure. To extract this infor-
568 mation, the script first checked whether the read carried an **SA:Z** tag. If present,
569 the tag string was parsed using the function **parse_sa_tag**, yielding metadata for
570 each alignment containing the reference name, mapped position, strand, mapping
571 quality, and number of mismatches.

572 After parsing, the function **sa_feature_stats** was applied to establish the fun-
573 damental split indicators, **has_sa** and **sa_count**. Along with these initial counts,
574 the function aggregated metrics related to the structure and reliability of the
575 split alignments, including the number of alignment segments, strand consistency,
576 minimum, maximum, and mean distance between split segments, and summary
577 statistics of mapping quality and mismatch counts across segments.

578 **K-mer Composition Difference**

579 Comparing k-mer frequency profiles between the left and right halves of a read
580 allows for the detection of abrupt compositional shifts, independent of alignment
581 information.

582 The script implemented this by inferring a likely junction breakpoint using the
583 function `infer_breakpoints`, prioritizing the boundaries defined by soft-clipping
584 operations. If no clipping was present, the midpoint of the alignment or the read
585 length was used as a fallback. The read sequence was then divided into left and
586 right segments at this inferred breakpoint, and k-mer frequency profiles ($k =$
587 6) were generated for both halves, ignoring any k-mers containing ambiguous N
588 bases. The resulting k-mer frequency vectors were normalised and compared using
589 the functions `cosine_difference` and `js_divergence` to quantify compositional
590 discontinuity across the inferred breakpoint.

591 **Microhomology**

592 The process of extracting the microhomology feature also started by using
593 `infer_breakpoints` to identify a candidate junction. Once a breakpoint was
594 established, the script scanned a ± 40 base-pair window surrounding the break-
595 point and applied the function `longest_suffix_prefix_overlap` to identify the
596 longest exact suffix-prefix overlap between the left and right read segments. This
597 overlap, representing consecutive bases shared at the junction, was recorded as
598 `microhomology_length` in the dataset. The 40 base-pair window was chosen
599 to ensure that short shared sequences at or near the breakpoint were captured

600 without including distant sequences that are unlikely to be mechanistically
601 related.

602 Additionally, the GC content of the overlapping sequence was calculated using
603 the function `gc_content`, which counts guanine (G) and cytosine (C) bases within
604 the detected microhomology and divides by the total length, yielding a proportion
605 between 0 and 1 that was stored under the `microhomology_gc` attribute. Micro-
606 homology was quantified using a 3–20 bp window, consistent with values reported
607 in prior research on PCR-induced chimeras. A k-mer length of 6 was used to cap-
608 ture patterns within the 40 bp window surrounding each breakpoint, providing
609 sufficient resolution to detect informative sequence shifts.

610 3.1.3 Machine Learning Model Development

611 After feature extraction, the per-read feature matrices for clean and chimeric
612 reads were merged into a single dataset. Each row corresponded to one paired-
613 end read, and columns encoded alignment-structure features (e.g., supplementary
614 alignment count and spacing between segments), CIGAR-derived soft-clipping
615 statistics (e.g., left and right soft-clipped length, total clipped bases), k-mer com-
616 position discontinuity between read segments, microhomology descriptors near
617 candidate junctions, and alignment quality (e.g., mapping quality). The result-
618 ing feature set comprised 23 numeric features and was restricted to quantities
619 that can be computed from standard BAM/FASTQ files in typical mitochondrial
620 sequencing workflows.

621 The labelled dataset was randomly partitioned into training (80%) and test

622 (20%) subsets using stratified sampling to preserve the 1:1 ratio of clean to
623 chimeric reads. Model development and evaluation were implemented in Python
624 (Version 3.11) using the `scikit-learn`, `xgboost`, `lightgbm`, and `catboost` li-
625 braries. A broad panel of classification algorithms was then benchmarked on the
626 training data to obtain a fair comparison of different model families under identical
627 feature conditions. The panel included a trivial dummy classifier, L_2 -regularized
628 logistic regression, a calibrated linear support vector machine (SVM), k -nearest
629 neighbours, Gaussian Naïve Bayes, decision-tree ensembles (Random Forest, Ex-
630 tremely Randomized Trees, and Bagging with decision trees), gradient boosting
631 methods (Gradient Boosting, XGBoost, LightGBM, and CatBoost), and a shallow
632 multilayer perceptron (MLP).

633 For each model, five-fold stratified cross-validation was performed on the train-
634 ing set. In every fold, four-fifths of the data were used for fitting and the remaining
635 one-fifth for validation. Mean cross-validation accuracy, precision, recall, F1-score
636 for the chimeric class, and area under the receiver operating characteristic curve
637 (ROC–AUC) were computed to summarize performance and rank candidate meth-
638 ods. This baseline screen allowed comparison of linear, probabilistic, neural, and
639 ensemble-based approaches and identified tree-based ensemble and boosting mod-
640 els as consistently strong performers relative to simpler baselines.

641 **3.1.4 Model Benchmarking, Hyperparameter Optimiza- 642 tion, and Evaluation**

643 Model selection and refinement proceeded in two stages. First, the cross-validation
644 results from the broad panel were used to identify a subset of competitive mod-

els for more detailed optimization. Specifically, ten model families were carried forward: L_2 -regularized logistic regression, calibrated linear SVM, Random Forest, ExtraTrees, Gradient Boosting, XGBoost, LightGBM, CatBoost, Bagging with decision trees, and a shallow MLP. This subset spans both linear and non-linear decision boundaries, but emphasizes ensemble and boosting methods, which showed superior F1 and ROC–AUC in the initial benchmark.

Second, hyperparameter optimization was conducted for each of the ten selected models using randomized search with five-fold stratified cross-validation (`RandomizedSearchCV`). For tree-based ensembles, the search space included the number of trees, maximum depth, minimum samples per split and per leaf, and the fraction of features considered at each split. For boosting methods, key hyperparameters such as the number of boosting iterations, learning rate, tree depth, subsampling rate, and column subsampling rate were tuned. For the MLP, the number and size of hidden layers, learning rate, and L_2 -regularization strength were varied. In all cases, the primary optimisation criterion was the F1-score of the chimeric class, averaged across folds.

For each model family, the hyperparameter configuration with the highest mean cross-validation F1-score was selected as the best-tuned estimator. These tuned models were then refitted on the full training set and evaluated once on the held-out test set to obtain unbiased estimates of performance. Test-set metrics included accuracy, precision, recall, F1-score for the chimeric class, and ROC–AUC. Confusion matrices and ROC curves were generated for the top-performing models to characterise common error modes, such as false negatives (missed chimeric reads) and false positives (clean reads incorrectly labelled as chimeric). The final model or small set of models for downstream interpretation was chosen based on

⁶⁷⁰ a combination of test-set F1-score and ROC-AUC.

671 3.1.5 Feature Importance, Feature Selection, and Inter- 672 pretation

To relate model decisions to biologically meaningful signals, feature-importance analyses were performed on the best-performing tree-based models. Two complementary approaches were used. First, built-in importance measures from ensemble methods (e.g., split-based importances in Random Forest and Gradient Boosting) were examined to obtain an initial ranking of features based on their contribution to reducing impurity. Second, model-agnostic permutation importance was computed on the test set by repeatedly permuting each feature column while keeping all others fixed and measuring the resulting decrease in F1-score. Features whose permutation led to a larger performance drop were interpreted as more influential for chimera detection.

For interpretability, individual features were grouped into conceptual families:

- (i) supplementary alignment and alignment-structure features (e.g., SA count, spacing between alignment segments, strand consistency), (ii) soft-clipping features (e.g., left and right soft-clipped length, total clipped bases, inferred break-point position), (iii) k-mer composition discontinuity features (e.g., cosine distance and Jensen–Shannon divergence between k-mer profiles of read segments), (iv) microhomology descriptors (e.g., microhomology length and local GC content around putative breakpoints), and (v) other alignment quality features (e.g., mapping quality). This analysis provided a basis for interpreting the trained models in terms of known mechanisms of PCR-induced template switching and for iden-

693 tifying which alignment-based and sequence-derived cues are most informative for
694 distinguishing chimeric from clean mitochondrial reads.

695 Building on these importance results, an explicit feature selection step was
696 implemented using CatBoost as the reference model, since it was among the top-
697 performing classifiers. Permutation importance scores were re-estimated for Cat-
698 Boost on the held-out test set using the F1-score of the chimeric class as the
699 scoring function. Negative importance scores, which indicate that permuting a
700 feature did not reliably harm performance, were set to zero and interpreted as
701 noise. The remaining non-negative importances were sorted in descending order
702 and converted into a cumulative importance curve by expressing each feature's
703 importance as a fraction of the total positive importance.

704 A compact feature subset was then defined by selecting the smallest number of
705 features whose cumulative importance reached at least 95% of the total positive
706 importance. This procedure yielded a reduced set of four strongly predictive
707 variables dominated by soft-clipping and k-mer divergence metrics (for example,
708 total clipped bases and k-mer divergence between read halves).

709 To quantify the impact of this reduction, CatBoost was retrained using only
710 the selected feature subset, with the same tuned hyperparameters as the full 23-
711 feature model, and evaluated on the held-out test set. Performance of the reduced
712 model was then compared to that of the full model in terms of F1-score and ROC–
713 AUC to assess whether dimensionality could be reduced without appreciable loss
714 in predictive accuracy.

715 In addition, an ablation experiment was performed to specifically evaluate
716 the contribution of explicit microhomology features. The microhomology vari-

ables (`microhomology_length` and `microhomology_gc`) were removed from the full feature set to obtain a 21-feature configuration. CatBoost was refitted on this microhomology-ablated feature set, using the same tuned hyperparameters, and evaluated on the held-out test set. Comparing the full, reduced-subset, and microhomology-ablated variants allowed the study to quantify both the degree of redundancy among features and the practical contribution of microhomology to classification accuracy.

Taken together, the feature importance and feature selection analyses provided a more parsimonious model variant and a clearer interpretation of which alignment-based and sequence-derived signals are most informative for detecting PCR-induced chimeras.

3.1.6 Validation and Testing

Validation involved both internal and external evaluations. Internal validation was achieved through five-fold stratified cross-validation on the training data to verify model generalization and reduce variance due to random sampling. External testing was performed on the 20% hold-out dataset from the simulated reads, providing an unbiased assessment of model generalization. Feature extraction and preprocessing were applied consistently across all splits.

Comparative evaluation was performed across all candidate algorithms and CatBoost feature-set variants to determine which models demonstrated the highest predictive performance and computational efficiency under identical data conditions. Their metrics were compared to identify which algorithms and feature

739 configurations were most suitable for further refinement and potential integration
740 into downstream mitochondrial assembly workflows.

741 **3.1.7 Documentation**

742 Comprehensive documentation was maintained throughout the study to ensure
743 transparency and reproducibility. All stages of the research, including data gath-
744 ering, preprocessing, feature extraction, model training, feature selection, and
745 validation, were systematically recorded in a `README` file in the GitHub reposi-
746 tory. For each analytical step, the corresponding parameters, software versions,
747 and command line scripts were documented to enable exact replication of results.

748 The repository structure followed standard research data management prac-
749 tices, with clear directories for datasets and scripts. Computational environments
750 were standardised using Conda, with an environment file (`environment.yml`)
751 specifying dependencies and package versions to maintain consistency across sys-
752 tems.

753 For manuscript preparation and supplementary materials, Overleaf (LATEX)
754 was used to produce publication-quality formatting and consistent referencing.

755 **3.2 Calendar of Activities**

756 Table 3.1 presents the project timeline in the form of a Gantt chart, where each
757 bullet point corresponds to approximately one week of planned activity.

Table 3.1: Timetable of activities.

Activities (2025)	Nov	Dec	Jan	Feb	Mar	Apr	May
Data Collection and Simulation	• • • •						
Feature Extraction Pipeline	•	•					
Machine Learning Development		•	• •	• • • •	• • • •	• •	
Testing and Validation						• •	• • • •
Documentation	• • • •	• • • •	• • • •	• • • •	• • • •	• • • •	• • • •

758 **Chapter 4**

759 **Results and Discussion**

760 This chapter presents the performance of the proposed feature set and machine
761 learning models for detecting PCR-induced chimeric reads in simulated mito-
762 chondrial Illumina data. The behaviour of the extracted features is first examined
763 through descriptive and correlation analyses, followed by a comparison of baseline
764 and tuned classifiers. The chapter then examines model performance in detail and
765 investigates the contribution of individual features and feature families, including
766 the impact of feature selection on classification performance.

767 The final dataset contained 31,986 reads for training and 7,997 reads for test-
768 ing, with classes balanced (approximately 4,000 clean and 4,000 chimeric reads in
769 the test split).

770 **4.1 Descriptive Analysis of Features**

771 **4.1.1 Summary Statistics Per Class**

772 Summary statistics were computed separately for clean reads (class 0) and
773 chimeric reads (class 1) to characterize the distributional behavior of the features.
774 For each feature, the mean, standard deviation, median, first and third quartiles
775 (Q1, Q3), interquartile range (IQR), minimum, maximum, and sample size (n)
776 were calculated.

777 Only a subset of the features is summarized in the main text to highlight key
778 trends, and not all summary statistics columns are shown for brevity. The com-
779 plete set of per-class summary statistics for all features is provided in Appendix A
780 (Table A.1).

781 **Alignment and Supplementary Alignment Features**

782 Features related to supplementary alignments show strong separation between
783 classes. Chimeric reads frequently exhibit supplementary alignments, reflected
784 by higher values of `has_sa`, `sa_count`, and `num_segments`, whereas clean reads
785 consistently show a single alignment segment with no supplementary mappings.
786 Table 4.1 shows that `has_sa` is present in chimeric reads (mean = 0.406) but absent
787 in clean reads (mean = 0.000), while `num_segments` increases from a constant value
788 of 1.000 in clean reads to a mean of 1.406 in chimeric reads. These patterns align
789 with the expected structure of chimeric reads and indicate that alignment-based
790 features are highly informative.

791 **Clipping-Based Features**

792 Clipping-related features, including `softclip_left`, `softclip_right`, and
793 `total_clipped_bases`, display higher values and broader distributions in chimeric
794 reads. In chimeric reads, `total_clipped_bases` reaches 25.44 on average, with a
795 median of 19.0 and an IQR of 48.0, while `softclip_left` and `softclip_right`
796 have averages of 12.55 and 12.90, medians of 0.0, and IQRs of 19.0. Clean
797 reads maintain values near zero across all these metrics. These patterns indi-
798 cate substantial clipping and increased variability in chimeric reads, reflecting
799 junction-like alignment fragmentation, whereas clean reads remain unaltered.

800 **K-mer Distribution Features**

801 K-mer-based features, including `kmer_js_divergence` and `kmer_cosine_diff`,
802 show only minor differences between clean and chimeric reads. In chimeric
803 reads, `kmer_js_divergence` has a mean of 0.974 with a median of 0.986, and
804 `kmer_cosine_diff` has a mean of 0.974 with a median of 0.986. Clean reads show
805 similar values, with `kmer_js_divergence` at 0.976 with a median of 0.986, and
806 `kmer_cosine_diff` at 0.976 with a median of 0.986. The close similarity of the
807 means, medians, and overall ranges of values indicates that these features alone
808 provide limited ability to distinguish clean from chimeric reads.

809 **Microhomology Features**

810 Microhomology-related features, including `microhomology_length` and
811 `microhomology_gc`, exhibit nearly identical summary statistics between clean

812 and chimeric reads. Most reads in both classes have short or zero-length micro-
813 homologies. Table 4.1 shows that `microhomology_gc` has a mean of 0.172 and
814 a median of 0.0 in both clean and chimeric reads, while `microhomology_length`
815 averages 0.458 with a median of 0.0 in chimeric reads and 0.462 with a median
816 of 0.0 in clean reads. These values indicate that microhomology features alone
817 provide limited discriminatory power and are more appropriately considered as
818 supporting evidence.

819 Overall, the summary statistics indicate that alignment-based and clipping-
820 based features provide the strongest class separation, k-mer features contribute
821 limited but complementary signal, and microhomology features exhibit minimal
822 discriminative power on their own. These observations motivate the combined
823 multi-feature approach used in subsequent modeling and evaluation.

Table 4.1: Summary statistics of selected key features by class.

Feature	Class	Mean	Std	Median	IQR
has_sa	chimeric	0.406	0.491	0.0	1.0
has_sa	clean	0.000	0.000	0.0	0.0
num_segments	chimeric	1.406	0.491	1.0	1.0
num_segments	clean	1.000	0.000	1.0	0.0
softclip_left	chimeric	12.55	21.90	0.0	19.0
softclip_left	clean	0.23	1.54	0.0	0.0
softclip_right	chimeric	12.90	22.12	0.0	19.0
softclip_right	clean	0.21	1.51	0.0	0.0
total_clipped_bases	chimeric	25.44	25.48	19.0	48.0
total_clipped_bases	clean	0.44	2.16	0.0	0.0
kmer_js_divergence	chimeric	0.974	0.025	0.986	0.043
kmer_js_divergence	clean	0.976	0.025	0.986	0.040
kmer_cosine_diff	chimeric	0.974	0.026	0.986	0.042
kmer_cosine_diff	clean	0.976	0.025	0.986	0.041
microhomology_length	chimeric	0.458	0.755	0.0	1.0
microhomology_length	clean	0.462	0.758	0.0	1.0
microhomology_gc	chimeric	0.172	0.361	0.0	0.0
microhomology_gc	clean	0.172	0.361	0.0	0.0

824 Boxplots were generated for each feature, with the x-axis representing the
 825 class (clean reads and chimeric reads) and the y-axis representing the feature
 826 value. Figure 4.1 presents a panel of selected key features, while boxplots for all
 827 numeric features are provided in Appendix B.

828 For clipping-related features (`softclip_left`, `softclip_right`,
 829 and `total_clipped_bases`), chimeric reads exhibit higher medians and longer
 830 upper whiskers than clean reads, indicating increased variability and the presence
 831 of split alignments.

832 Supplementary alignment features (`has_sa` and `sa_count`), show that clean
 833 reads are largely zero, whereas chimeric reads display a wider distribution, re-

834 reflecting frequent supplementary alignments.

835 K-mer metrics (`kmer_js_divergence` and `kmer_cosine_diff`) show a slight
836 upward shift for chimeric reads, but substantial overlap with clean reads indicates
837 low discriminative power.

838 Microhomology features (`microhomology_length` and `microhomology_gc`)
839 have nearly overlapping distributions for both classes, consistent with their low
840 standalone predictive importance.

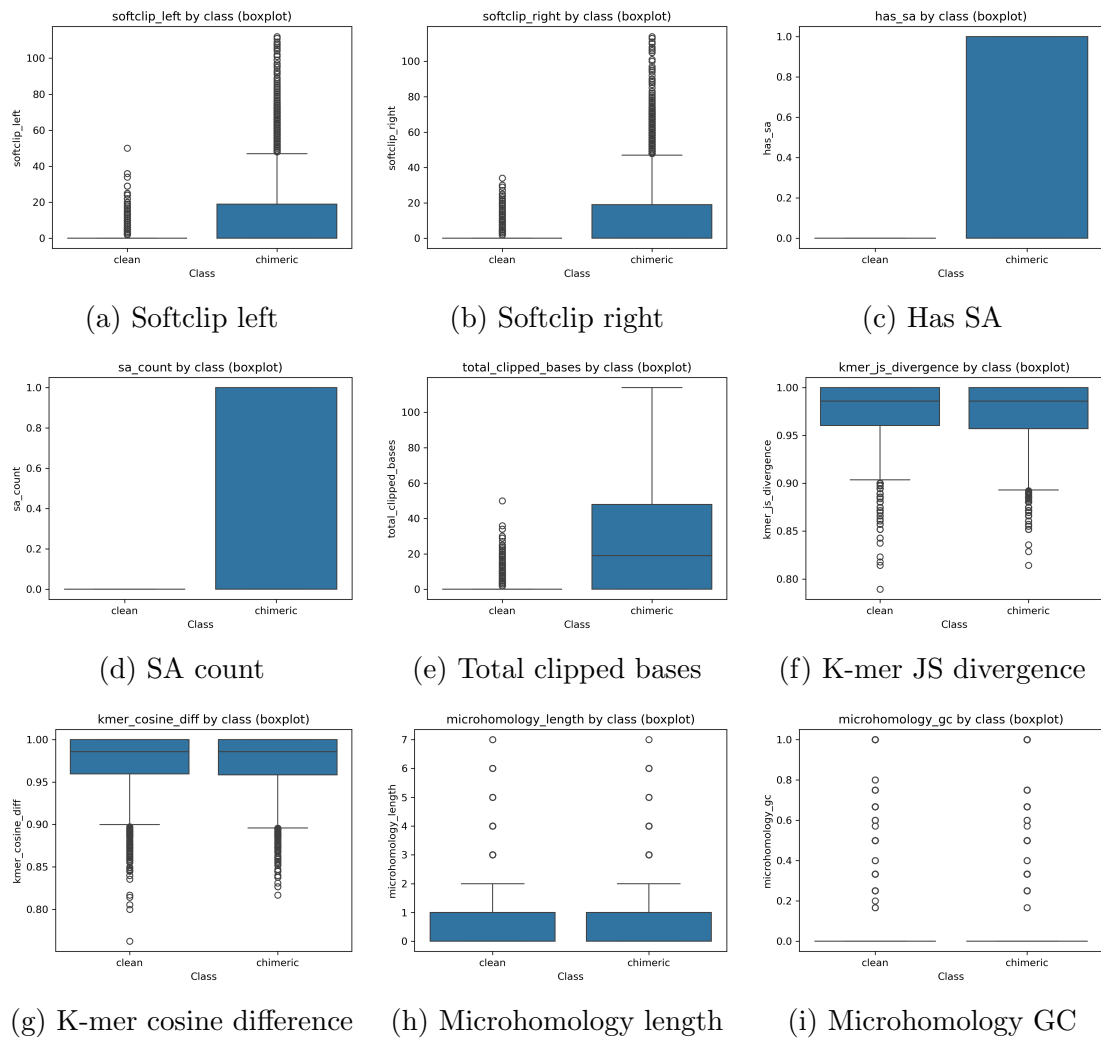


Figure 4.1: Boxplots of selected features for clean and chimeric reads.

841 4.1.2 Correlation Analysis of Extracted Features

842 A feature correlation heatmap (Figure 4.2) was generated to examine relationships
843 among the extracted variables and to identify patterns of redundancy and inde-
844 pendence within the feature set. The analysis shows that alignment-related and
845 clipping-related features form a strongly correlated cluster, including indicators
846 of supplementary alignments, alignment segment counts, positional differences,
847 and soft-clipping measures. These features capture related aspects of alignment
848 fragmentation, which is a known characteristic of chimeric reads, and several
849 show moderate correlations with the class label, supporting their relevance for
850 distinguishing chimeric from clean reads. In contrast, general read-quality and
851 alignment-quality metrics, such as read length, base quality, and mapping qual-
852 ity, exhibit weak correlations with most split-alignment features, indicating that
853 they provide distinct information rather than overlapping with alignment-derived
854 signals. Sequence-based features display a similar pattern of independence, as
855 k-mer divergence metrics show weak correlations with other feature groups, while
856 microhomology features exhibit generally low correlations with both alignment-
857 based and k-mer-based features. Overall, the correlation structure highlights in-
858 tentional redundancy within alignment-derived features and clear separation be-
859 tween feature families, supporting the use of features that capture different aspects
860 of chimeric read characteristics to improve chimera classification.

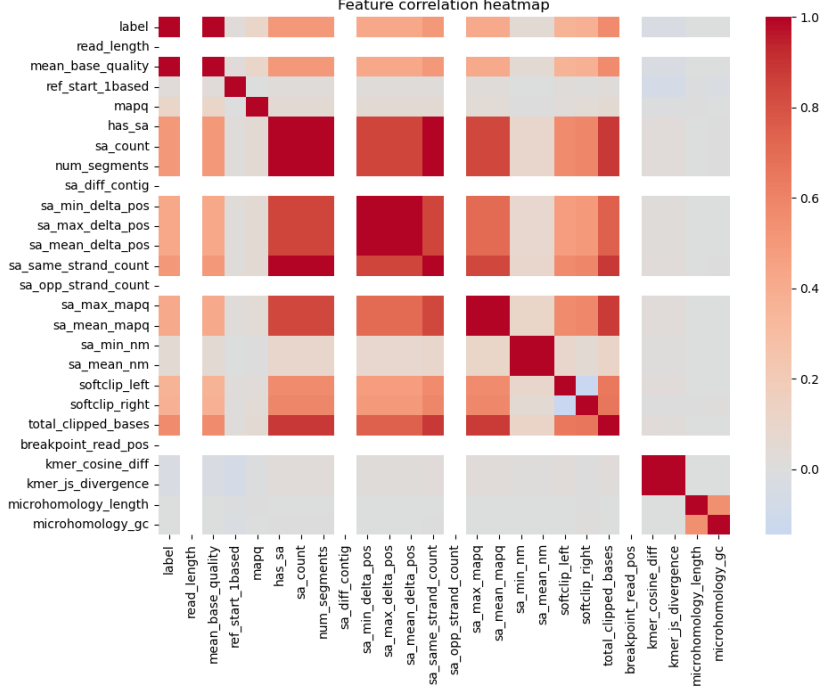


Figure 4.2: Feature correlation heatmap showing relationships among alignment-derived and sequence-derived features.

861 4.2 Baseline Classification Performance

862 Table 4.2 summarises the performance of eleven classifiers trained on the engi-
 863 neered feature set using five-fold cross-validation and evaluated on the held-out
 864 test set. All models were optimised using default hyperparameters, without ded-
 865 icated tuning.

866 The dummy baseline, which always predicts the same class regardless of the
 867 input features, achieved an accuracy of 0.50 and test F1-score of 0.67. This re-
 868 flects the balanced class distribution and provides a lower bound for meaningful
 869 performance.

870 Across other models, test F1-scores clustered in a narrow band between ap-
 871 proximately 0.74 and 0.77 and ROC–AUC values between 0.82 and 0.84. Gradi-
 872 ent boosting, CatBoost, LightGBM, XGBoost, bagging trees, random forest, and
 873 multilayer perceptron (MLP) all produced very similar scores, with CatBoost and
 874 gradient boosting slightly ahead (test F1 \approx 0.77, ROC–AUC \approx 0.84). Linear
 875 models (logistic regression and calibrated linear SVM) performed only marginally
 876 worse (test F1 \approx 0.74), while Gaussian Naive Bayes lagged behind with substan-
 877 tially lower F1 (\approx 0.65) despite very high precision for the chimeric class.

Table 4.2: Performance of baseline classifiers on the held-out test set.

model	test_accuracy	test_precision	test_recall	test_f1	test_roc_auc
dummy_baseline	0.500000	0.500000	1.000000	0.667000	0.500000
logreg_l2	0.789000	0.945000	0.614000	0.744000	0.821000
linear_svm_calibrated	0.789000	0.945000	0.614000	0.744000	0.820000
random_forest	0.788000	0.894000	0.654000	0.755000	0.834000
extra_trees	0.788000	0.901000	0.647000	0.753000	0.824000
gradient_boosting	0.802000	0.936000	0.648000	0.766000	0.840000
xgboost	0.800000	0.929000	0.650000	0.765000	0.839000
lightgbm	0.799000	0.926000	0.650000	0.764000	0.838000
catboost	0.803000	0.936000	0.650000	0.767000	0.839000
knn	0.782000	0.892000	0.642000	0.747000	0.815000
gaussian_nb	0.741000	0.996000	0.483000	0.651000	0.819000
bagging_trees	0.792000	0.900000	0.657000	0.760000	0.837000
mlp	0.789000	0.931000	0.625000	0.748000	0.819000

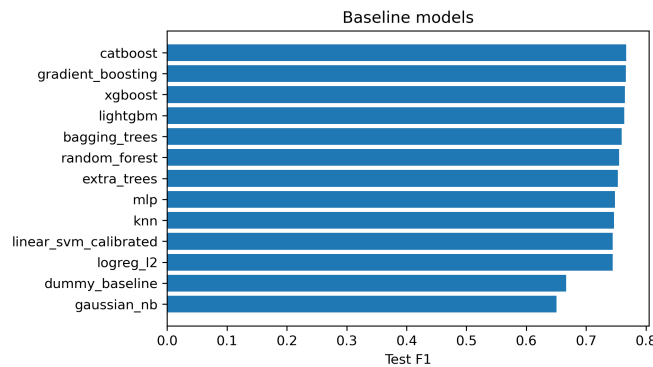


Figure 4.3: Test F1 of all baseline classifiers, showing that no single model clearly dominates and several achieve comparable performance.

878 4.3 Effect of Hyperparameter Tuning

879 To assess whether performance could be improved further, ten model families un-
880 derwent randomised hyperparameter search. The tuned metrics are summarised
881 in Table 4.3. Overall, tuning yielded modest but consistent gains for tree-based en-
882 sembles and boosting methods, while leaving linear models essentially unchanged
883 or slightly worse.

884 CatBoost, gradient boosting, LightGBM, XGBoost, random forest, bagging
885 trees, and MLP all experienced small increases in test F1 (typically $\Delta F1 \approx 0.002$ –
886 0.009) and ROC–AUC (up to $\Delta AUC \approx 0.008$). After tuning, CatBoost remained
887 the best performer with test accuracy 0.80, precision 0.92, recall 0.66, F1-score
888 0.77, and ROC–AUC 0.84. Gradient boosting achieved almost identical perfor-
889 mance (F1 0.77, AUC 0.84). Random forest and bagging trees also improved to
890 F1 scores around 0.76 with AUC ≈ 0.84 .

Table 4.3: Performance of tuned classifiers on the held-out test set.

model	test_accuracy	test_precision	test_recall	test_f1	test_roc_auc
logreg_l2_tuned	0.788000	0.946000	0.612000	0.743000	0.818000
linear_svm_calibrated_tuned	0.788000	0.944000	0.612000	0.743000	0.818000
random_forest_tuned	0.797000	0.915000	0.655000	0.763000	0.842000
extra_trees_tuned	0.794000	0.910000	0.652000	0.760000	0.837000
gradient_boosting_tuned	0.802000	0.928000	0.654000	0.767000	0.843000
xgboost_tuned	0.799000	0.922000	0.653000	0.765000	0.839000
lightgbm_tuned	0.801000	0.930000	0.651000	0.766000	0.842000
catboost_tuned	0.802000	0.924000	0.658000	0.769000	0.844000
bagging_trees_tuned	0.798000	0.922000	0.650000	0.763000	0.842000
mlp_tuned	0.790000	0.934000	0.625000	0.749000	0.821000

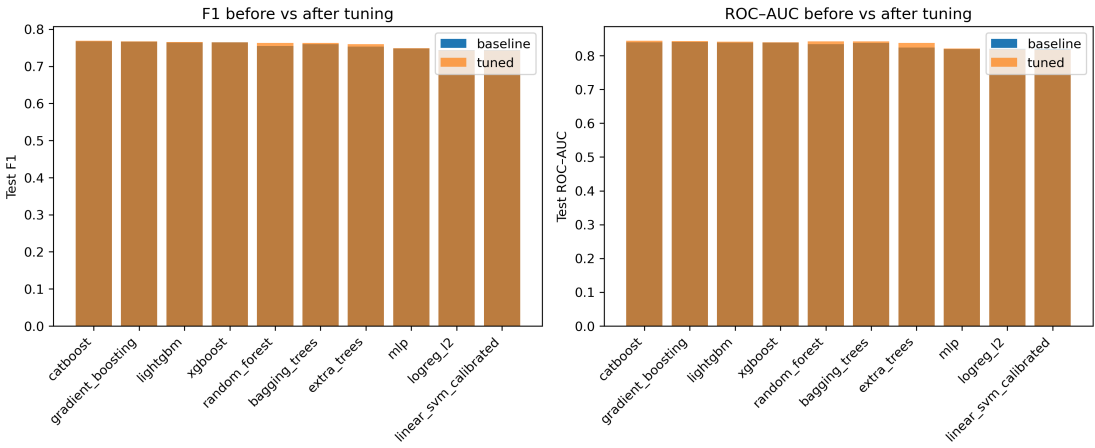


Figure 4.4: Comparison of test F1 (left) and ROC–AUC (right) for baseline and tuned models.

891 Because improvements are small and within cross-validation variability, tun-
 892 ing was interpreted as stabilising and slightly refining the models rather than
 893 completely altering their behaviour or their relative ranking.

894 4.4 Detailed Evaluation of Representative Mod- 895 els

896 For interpretability and diversity, four tuned models were selected for deeper
 897 analysis: CatBoost (best-performing boosted tree), scikit-learn gradient boost-
 898 ing (canonical gradient-boosting implementation), random forest (non-boosted
 899 ensemble baseline), and L_2 -regularised logistic regression (linear baseline). All
 900 models were trained on the engineered feature set and evaluated on the same
 901 held-out test data.

902 4.4.1 Confusion Matrices and Error Patterns

903 Classification reports and confusion matrices for the four models reveal consistent
904 patterns. CatBoost and gradient boosting both reached overall accuracy of ap-
905 proximately 0.80 with similar macro-averaged F1 scores (~ 0.80). For CatBoost,
906 precision and recall for clean reads were 0.73 and 0.95, respectively, while for
907 chimeric reads they were 0.92 and 0.66 ($F1 = 0.77$). Gradient boosting showed
908 nearly identical trade-offs.

909 Random forest attained slightly lower accuracy (0.80) and chimeric F1 (0.76),
910 whereas logistic regression achieved the lowest accuracy among the four (0.79)
911 and chimeric F1 (0.74), although it provided the highest chimeric precision (0.95)
912 at the cost of lower recall (0.61).

913 Across all models, errors were asymmetric. False negatives (chimeric reads pre-
914 dicted as clean) were more frequent than false positives. For example, CatBoost
915 misclassified 1,369 chimeric reads as clean but only 215 clean reads as chimeric.
916 This pattern indicates that the models are conservative and prioritise avoiding
917 false chimera calls at the expense of missing some true chimeras. Consultation
918 with PGC Visayas indicated that this conservative behavior is generally accept-
919 able, though further evaluation and testing will be required to assess its impact
920 on downstream analyses.

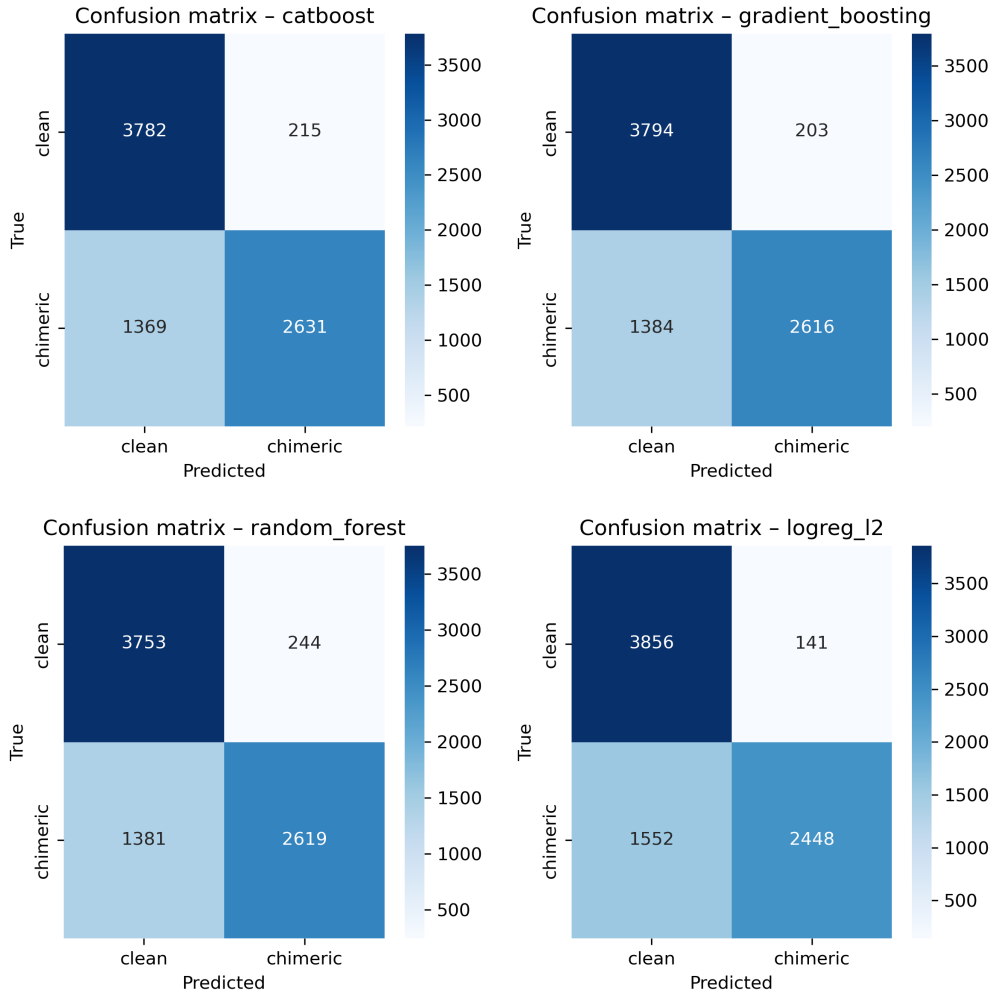


Figure 4.5: Confusion matrices for the four representative models on the held-out test set.

921 4.4.2 ROC and Precision–Recall Curves

922 Receiver operating characteristic (ROC) and precision–recall (PR) curves as
 923 shown in Figure 4.6 further support the similarity among the top models. The
 924 three tree-based ensembles (CatBoost, gradient boosting, random forest) achieved
 925 ROC–AUC values of approximately 0.84 and average precision (AP) around 0.88.

926 Logistic regression performed slightly worse ($AUC \approx 0.82$, $AP \approx 0.87$) but still
927 substantially better than the dummy baseline.

928 The PR curves show that precision remains above 0.9 across a broad range
929 of recall values (up to roughly 0.5–0.6), after which precision gradually declines.
930 This behaviour indicates that the models can assign very high confidence to a
931 subset of chimeric reads, while more ambiguous reads can only be recovered by
932 accepting lower precision.

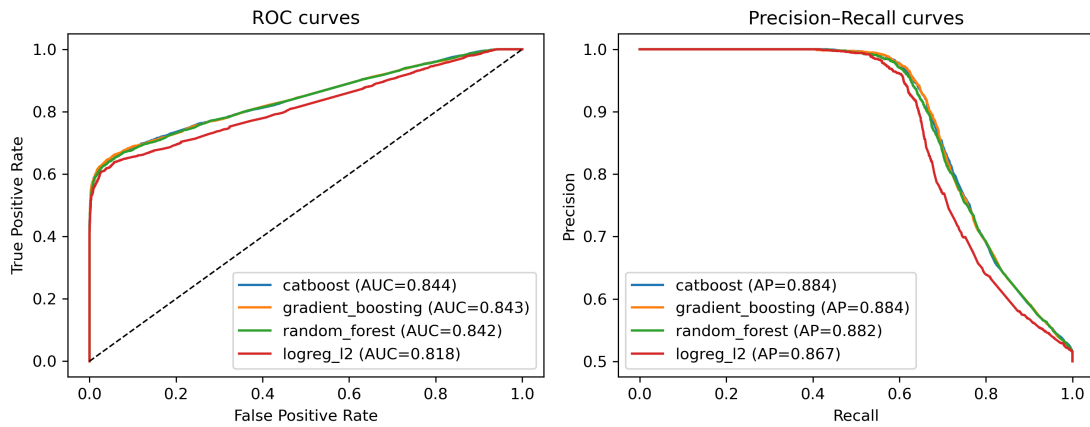


Figure 4.6: ROC (left) and precision–recall (right) curves for the four representative models on the held-out test set.

933 4.5 Feature Importance

934 4.5.1 Permutation Importance of Individual Features

935 To understand how each classifier made predictions, feature importance was quan-
936 tified using permutation importance. This analysis was applied to four represen-
937 tative models: CatBoost, Gradient Boosting, Random Forest, and L₂-regularized

938 Logistic Regression.

939 As shown in Figure 4.7, the total number of clipped bases consistently pro-
940 vides a strong predictive signal, particularly in Random Forest, Gradient Boosting,
941 and L₂-regularized Logistic Regression. CatBoost differs by assigning the highest
942 importance to k-mer divergence metrics such as `kmer_js_divergence`, which cap-
943 ture subtle sequence changes resulting from structural variants or PCR-induced
944 chimeras. Soft-clipping features (`softclip_left` and `softclip_right`) provide
945 more information around breakpoints, complementing these primary signals in all
946 models except Gradient Boosting. L₂-regularized Logistic Regression relies more
947 on alignment-based split-read metrics.

948 Overall, these results indicate that accurate detection of chimeric reads relies
949 on both alignment-based signals and k-mer compositional information. Explicit
950 microhomology features contribute minimally in this analysis, and combining both
951 alignment-based and sequence-level features enhances model sensitivity and speci-
952 ficity.

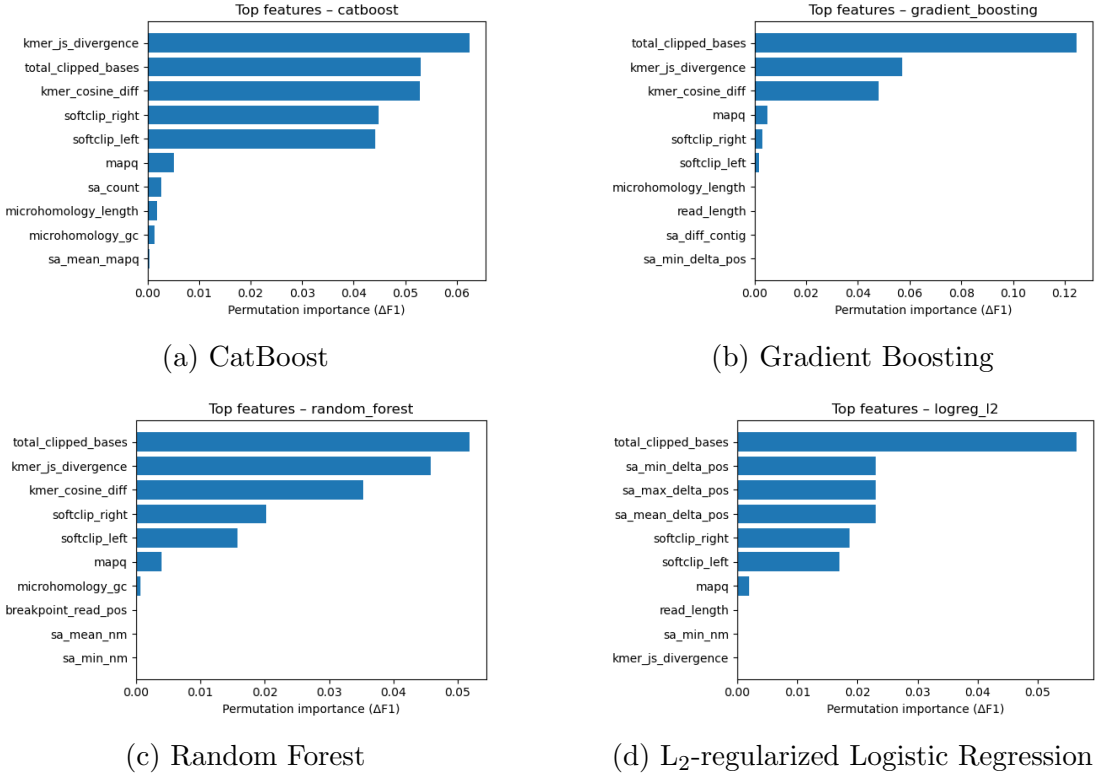


Figure 4.7: Permutation-based feature importance for four representative classifiers.

953 4.5.2 Feature Family Importance

954 To evaluate the contribution of broader signals, features were grouped into
 955 five families: SA_structure (supplementary alignment and segment met-
 956 rics, e.g., has_sa, sa_count, sa_min_delta_pos, sa_mean_nm, etc.), Clipping
 957 (softclip_left, softclip_right, total_clipped_bases, breakpoint_read_pos),
 958 Kmer_jump (kmer_cosine_diff, kmer_js_divergence), Micro_homology (microhomology_length, microhomology_gc), and Other (e.g., mapq).

960 Aggregated analyses reveal consistent patterns across models. In CatBoost,
 961 the Clipping family has the largest cumulative contribution (0.14), followed

962 by Kmer_jump (0.12), with Other features contributing minimally (0.005) and
963 SA_structure (0.003) and Micro_homology (0.003) providing minimal predictive
964 power. Gradient Boosting shows a similar trend, with Clipping (0.13) domi-
965 nating, Kmer_jump (0.11) secondary, and the remaining families contributing
966 negligibly. Random Forest integrates both Clipping (0.088) and Kmer_jump
967 (0.08) effectively, while SA_structure, Micro_homology, and Other remain minor
968 contributors. L₂-regularized Logistic Regression emphasizes Clipping (0.09)
969 and SA_structure (0.07), with Kmer_jump and Micro_homology having minimal
970 impact.

971 Both feature-level and aggregated analyses indicate that detection of chimeric
972 reads in this dataset relies primarily on alignment irregularities (Clipping) and
973 k-mer compositional shifts (Kmer_jump), which often arise from PCR-induced
974 template switching events, while explicit microhomology features contribute min-
975 imally.

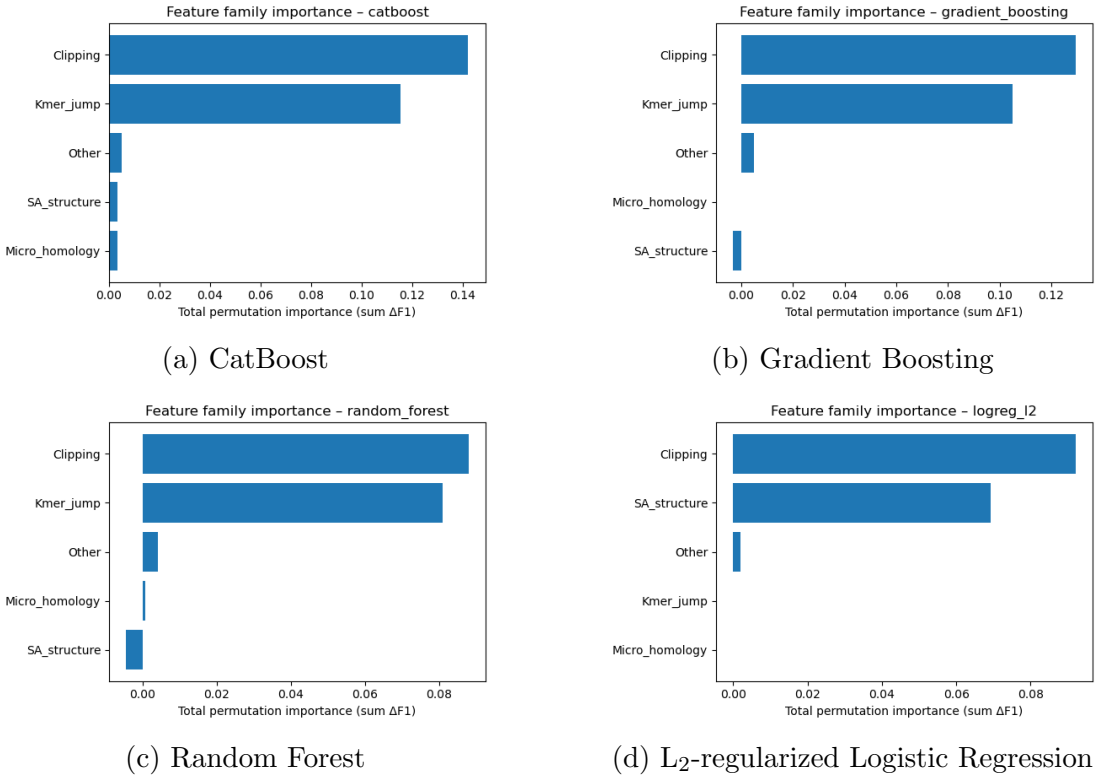


Figure 4.8: Aggregated feature family importance across four models.

976 4.6 Feature Selection

977 Feature selection was performed to identify the smallest subset reaching 95% cu-
 978 mulative importance. Three models were evaluated as references: the full model
 979 with all 23 features, a reduced model with the top- k features, and an ablation
 980 model excluding microhomology features, using a tuned CatBoost classifier to
 981 assess feature contributions and overall classification performance.

982 **4.6.1 Cumulative Importance Curve**

983 The cumulative importance curve was computed using the tuned CatBoost clas-
984 sifier. Figure 4.9 illustrates the contribution of features sorted by importance.
985 The curve rises steeply for the first few features and then gradually plateaus,
986 indicating that a small number of features capture most of the model’s pre-
987 dictive power. A cumulative importance of 95% is reached at $k = 4$ features,
988 which are `total_clipped_bases`, `kmer_js_divergence`, `kmer_cosine_diff`, and
989 `softclip_left`.

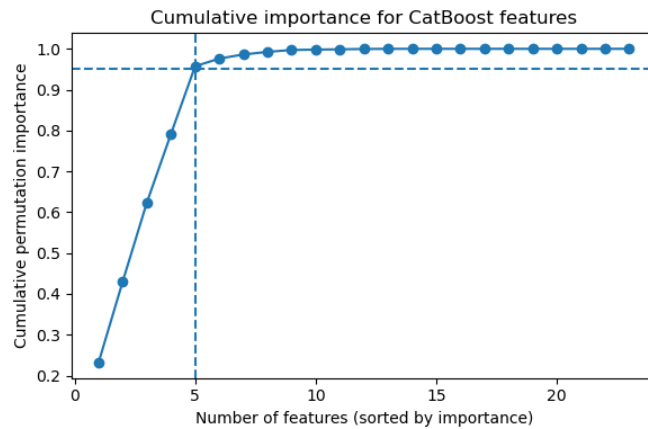


Figure 4.9: Cumulative importance curve of features sorted by importance.

990 **4.6.2 Performance Comparison Across Feature Sets**

991 Classification performance was compared across three feature sets using a tuned
992 CatBoost classifier. The full model, incorporating all 23 engineered features,
993 achieved an F1 score of 0.769 and a ROC–AUC of 0.844. A reduced model
994 using only the top four features (`total_clipped_bases`, `kmer_js_divergence`,
995 `kmer_cosine_diff`, and `softclip_left`) achieved nearly equivalent performance

996 with an F1 of 0.767 and a ROC–AUC of 0.835. An ablation model excluding mi-
 997 crohomology features (`microhomology_length` and `microhomology_gc`) also per-
 998 formed comparably, with an F1 of 0.768 and ROC–AUC of 0.845. These results
 999 indicate that clipping and k-mer features capture almost all predictive signal,
 1000 while microhomology features are largely redundant in this dataset.

Table 4.4: Test set performance of three feature set variants using tuned CatBoost.

Variant	No. of Features	Test F1	ROC–AUC
Full CatBoost	23	0.769	0.844
Selected (top-4)	4	0.767	0.835
No microhomology	21	0.768	0.845

1001 Figure 4.10 presents a bar chart comparing F1 and ROC–AUC across the
 1002 three variants, with the x-axis showing the model variants and two bars per group
 1003 representing the F1 and ROC–AUC values.

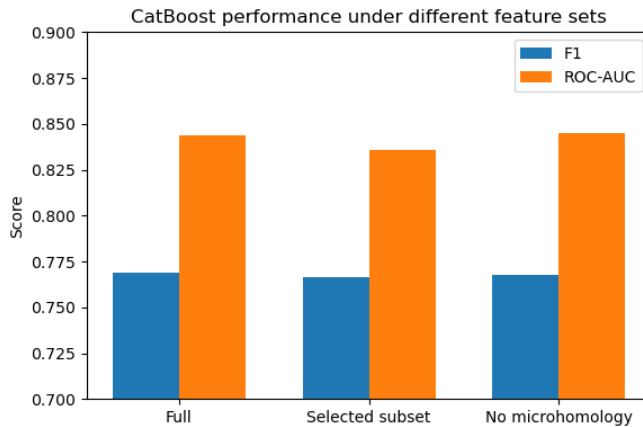


Figure 4.10: Comparison of F1 and ROC–AUC for the full, top-4 selected, and no-microhomology feature set variants.

1004 **4.6.3 Interpretation and Final Feature Set Choice**

1005 The full 23-feature model is retained as the primary configuration for the re-
1006 mainder of the study, while the four-feature subset serves as a lightweight al-
1007 ternative. Clipping features reflect alignment junctions and mapping disruptions
1008 typical of chimeric reads, and k-mer divergence captures changes in sequence com-
1009 position across breakpoints. Microhomology features appear largely redundant,
1010 as their signal is either indirectly represented by clipping and k-mer features or
1011 not strongly expressed in the simulation dataset.

1012 **4.7 Summary of Findings**

1013 All evaluated machine learning models substantially outperformed the dummy
1014 baseline, demonstrating that the engineered feature set contains meaningful
1015 signals for detecting PCR-induced chimeric reads. Across classifiers, the best-
1016 performing models achieved test F1-scores of approximately 0.77 and ROC–AUC
1017 values around 0.84 on held-out simulated mitochondrial reads, indicating reli-
1018 able discrimination between clean and chimeric sequences. Among the tested
1019 approaches, tree-based ensemble and boosting methods consistently showed the
1020 strongest and most stable performance. In particular, CatBoost and Gradient
1021 Boosting ranked among the top models across multiple evaluation metrics,
1022 both before and after hyperparameter tuning. These results suggest that non-
1023 linear ensemble methods are well suited to capturing the interaction between
1024 alignment-derived and sequence-derived features in this setting.

1025 Analysis of feature behaviour revealed clear differences in how effectively fea-

ture groups distinguished clean and chimeric reads. Alignment- and clipping-based features, such as soft-clipping measures and total clipped bases, showed strong separation between clean and chimeric reads and emerged as the most informative signals. K-mer divergence features provided additional but weaker separation, contributing complementary information beyond alignment irregularities. In contrast, microhomology features and several supplementary alignment (SA) structure metrics exhibited minimal class separation and contributed little to overall predictive performance.

Feature selection results further supported these observations. A reduced subset of four features, dominated by clipping-based and k-mer divergence metrics, achieved nearly identical performance to the full 23-feature model. Moreover, removing explicit microhomology features did not degrade performance and in some cases resulted in slightly improved metrics, suggesting that these features are largely redundant under the simulated conditions tested.

Overall, these findings suggest that alignment-based and k-mer-based features provide sufficient signal to detect PCR-induced chimeric reads in simulated mitochondrial data, supporting the use of a compact and interpretable machine learning approach as a pre-assembly chimera detection step.

1044 **Appendix A**

1045 **Complete Per-Class Summary**

1046 **Statistics**

Table A.1: Complete per-class summary statistics for all extracted features.

Feature	Class	Mean	Std	Median	Q1	Q3	IQR	Min	Max	n
breakpoint_read_pos	chimeric	75.000	0.000	75.000	75.000	75.000	0.000	75.000	75.000	20000
breakpoint_read_pos	clean	75.000	0.000	75.000	75.000	75.000	0.000	75.000	75.000	19983
has_sa	chimeric	0.406	0.491	0.000	0.000	1.000	1.000	0.000	1.000	20000
has_sa	clean	0.000	0.000	0.000	0.000	0.000	0.000	0.000	0.000	19983
kmer_cosine_diff	chimeric	0.974	0.026	0.986	0.958	1.000	0.042	0.817	1.000	20000
kmer_cosine_diff	clean	0.976	0.025	0.986	0.959	1.000	0.041	0.814	1.000	19983
kmer_js_divergence	chimeric	0.974	0.025	0.986	0.957	1.000	0.043	0.811	1.000	20000
kmer_js_divergence	clean	0.976	0.025	0.986	0.959	1.000	0.040	0.817	1.000	19983
mapq	chimeric	59.987	0.355	60.000	60.000	60.000	0.000	43.000	60.000	20000
mapq	clean	59.663	2.036	60.000	60.000	60.000	0.000	0.000	60.000	19983
mean_base_quality	chimeric	40.000	0.000	40.000	40.000	40.000	0.000	40.000	40.000	20000
mean_base_quality	clean	13.000	0.000	13.000	13.000	13.000	0.000	13.000	13.000	19983
microhomology_gc	chimeric	0.172	0.361	0.000	0.000	0.000	0.000	0.000	1.000	20000
microhomology_gc	clean	0.172	0.361	0.000	0.000	0.000	0.000	0.000	1.000	19983
microhomology_length	chimeric	0.458	0.755	0.000	0.000	1.000	1.000	0.000	5.000	20000
microhomology_length	clean	0.462	0.758	0.000	0.000	1.000	1.000	0.000	5.000	19983

Continued on next page

Feature	Class	Mean	Std	Median	Q1	Q3	IQR	Min	Max	n
num_segments	chimeric	1.406	0.491	1.000	1.000	2.000	1.000	1.000	2.000	20000
num_segments	clean	1.000	0.000	1.000	1.000	1.000	0.000	1.000	1.000	19983
read_length	chimeric	150.000	0.000	150.000	150.000	150.000	0.000	150.000	150.000	20000
read_length	clean	150.000	0.000	150.000	150.000	150.000	0.000	150.000	150.000	19983
ref_start_1based	chimeric	8428.635	4248.348	8433.000	5013.000	11786.250	6773.250	1.000	16521.000	20000
ref_start_1based	clean	8200.121	4626.918	8240.000	3639.000	11565.000	7926.000	1.000	16521.000	19983
sa_count	chimeric	0.406	0.491	0.000	0.000	1.000	1.000	0.000	1.000	20000
sa_count	clean	0.000	0.000	0.000	0.000	0.000	0.000	0.000	0.000	19983
sa_diff_contig	chimeric	0.000	0.000	0.000	0.000	0.000	0.000	0.000	0.000	20000
sa_diff_contig	clean	0.000	0.000	0.000	0.000	0.000	0.000	0.000	0.000	19983
sa_max_delta_pos	chimeric	1573.531	2364.996	0.000	0.000	2826.250	2826.250	0.000	16519.000	20000
sa_max_delta_pos	clean	0.000	0.000	0.000	0.000	0.000	0.000	0.000	0.000	19983
sa_max_mapq	chimeric	14.104	21.424	0.000	0.000	27.000	27.000	0.000	60.000	20000
sa_max_mapq	clean	0.000	0.000	0.000	0.000	0.000	0.000	0.000	0.000	19983
sa_mean_delta_pos	chimeric	1573.531	2364.996	0.000	0.000	2826.250	2826.250	0.000	16519.000	20000
sa_mean_delta_pos	clean	0.000	0.000	0.000	0.000	0.000	0.000	0.000	0.000	19983
sa_mean_mapq	chimeric	14.104	21.424	0.000	0.000	27.000	27.000	0.000	60.000	20000
sa_mean_mapq	clean	0.000	0.000	0.000	0.000	0.000	0.000	0.000	0.000	19983

Continued on next page

Feature	Class	Mean	Std	Median	Q1	Q3	IQR	Min	Max	n
sa_mean_nm	chimeric	0.022	0.319	0.000	0.000	0.000	0.000	0.000	6.000	20000
sa_mean_nm	clean	0.000	0.000	0.000	0.000	0.000	0.000	0.000	0.000	19983
sa_min_delta_pos	chimeric	1573.531	2364.996	0.000	0.000	2826.250	2826.250	0.000	16519.000	20000
sa_min_delta_pos	clean	0.000	0.000	0.000	0.000	0.000	0.000	0.000	0.000	19983
sa_min_nm	chimeric	0.022	0.319	0.000	0.000	0.000	0.000	0.000	6.000	20000
sa_min_nm	clean	0.000	0.000	0.000	0.000	0.000	0.000	0.000	0.000	19983
sa_opp_strand_count	chimeric	0.000	0.000	0.000	0.000	0.000	0.000	0.000	0.000	20000
sa_opp_strand_count	clean	0.000	0.000	0.000	0.000	0.000	0.000	0.000	0.000	19983
sa_same_strand_count	chimeric	0.406	0.491	0.000	0.000	1.000	1.000	0.000	1.000	20000
sa_same_strand_count	clean	0.000	0.000	0.000	0.000	0.000	0.000	0.000	0.000	19983
softclip_left	chimeric	12.546	21.898	0.000	0.000	19.000	19.000	0.000	150.000	20000
softclip_left	clean	0.225	1.543	0.000	0.000	0.000	0.000	0.000	56.000	19983
softclip_right	chimeric	12.896	22.123	0.000	0.000	19.000	19.000	0.000	150.000	20000
softclip_right	clean	0.212	1.513	0.000	0.000	0.000	0.000	0.000	55.000	19983
total_clipped_bases	chimeric	25.442	25.481	19.000	0.000	48.000	48.000	0.000	150.000	20000
total_clipped_bases	clean	0.437	2.157	0.000	0.000	0.000	0.000	0.000	110.000	19983

1048 **Appendix B**

1049 **Boxplots for All Numeric**

1050 **Features by Feature Family**

1051 **B.0.1 SA Structure (Supplementary Alignment and Seg-**
1052 **ment Metrics)**

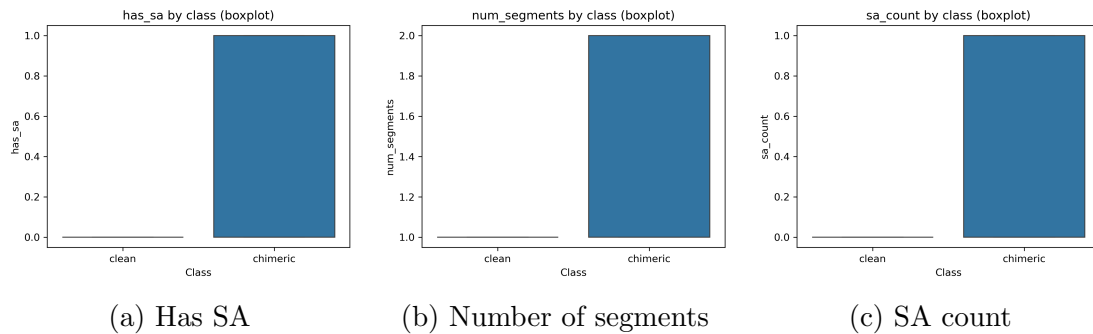


Figure B.1: Boxplots of SA Structure features by class (1/2).

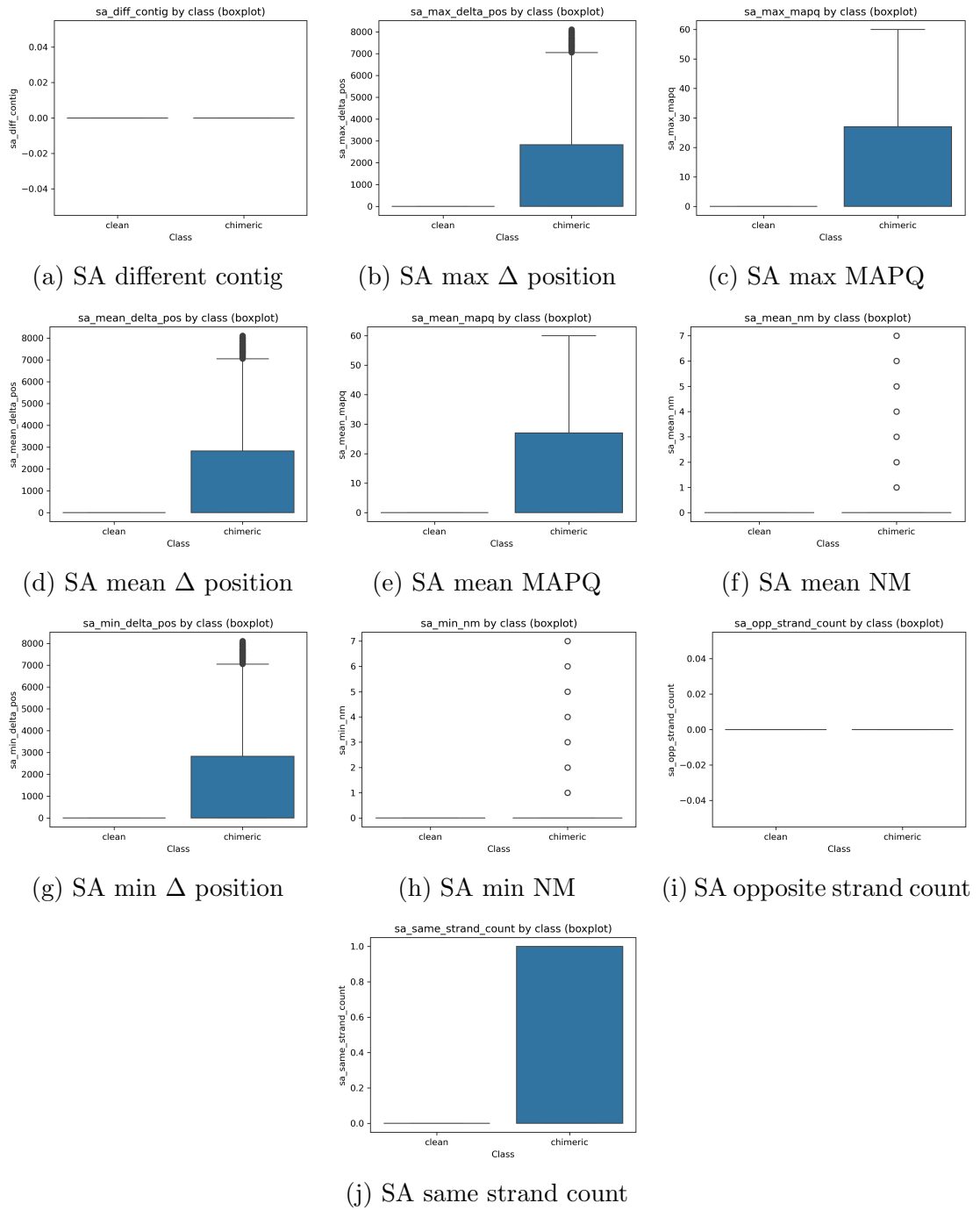


Figure B.2: Boxplots of SA Structure features by class (2/2).

1053 **B.0.2 Clipping-Based Features**

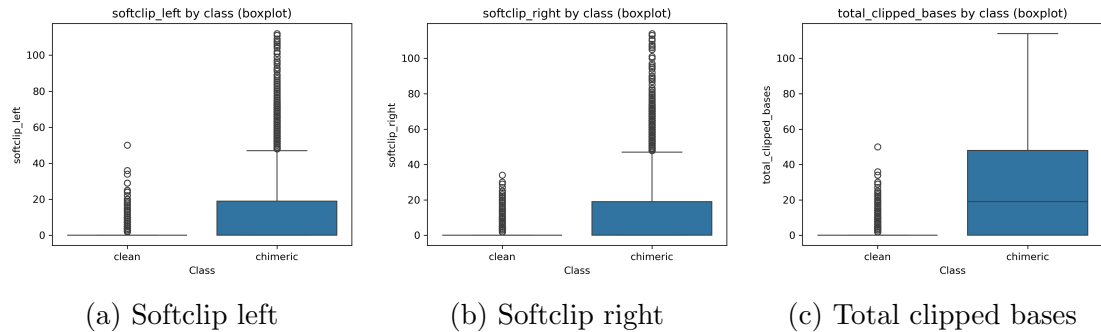


Figure B.3: Boxplots of clipping-based features by class.

1054 **B.0.3 K-mer Features**



Figure B.4: Boxplots of k-mer features by class.

1055 **B.0.4 Microhomology Features**



Figure B.5: Boxplots of microhomology features by class.

1056 **B.0.5 Others**

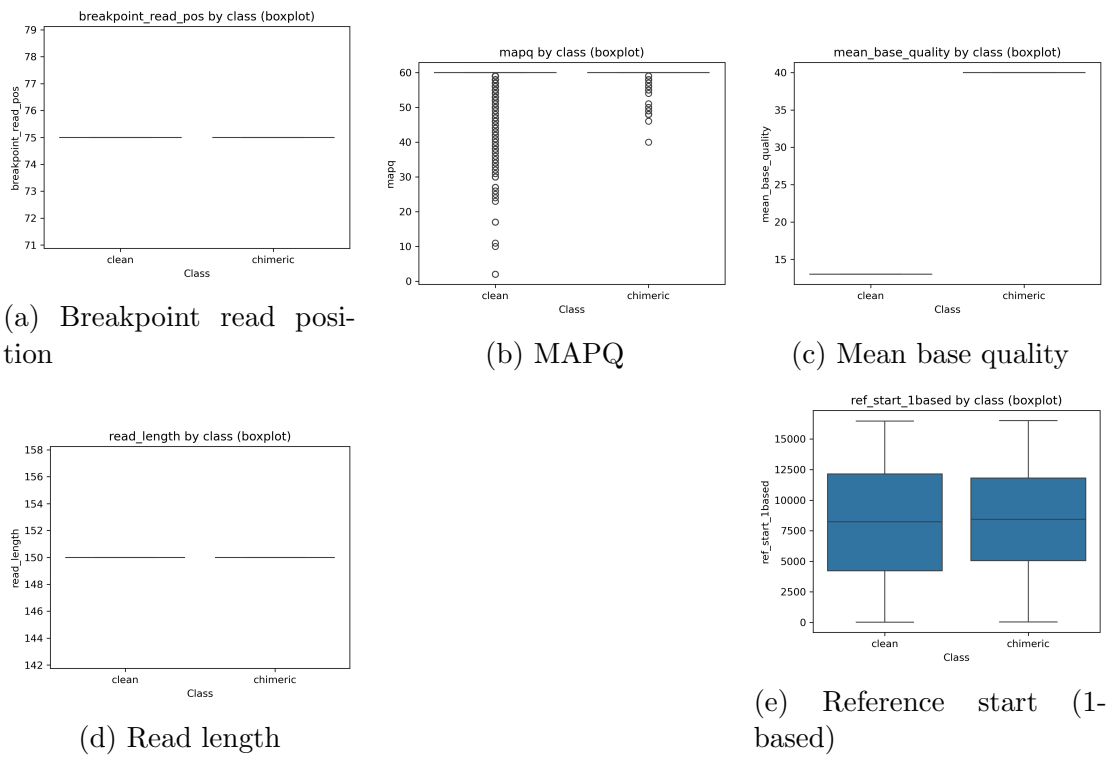


Figure B.6: Boxplots of other numeric features by class.

¹⁰⁵⁷ References

- 1058 Anderson, S., Bankier, A., Barrell, B., Bruijn, M., Coulson, A., Drouin, J., ...
1059 Young, I. (1981, 04). Sequence and organization of the human mitochondrial
1060 genome. *Nature*, *290*, 457-465. doi: 10.1038/290457a0
- 1061 Arango, G., Garner, E., Pruden, A., Heath, L., Vikesland, P., & Zhang, L. (2018,
1062 02). Deeparg: A deep learning approach for predicting antibiotic resistance
1063 genes from metagenomic data. *Microbiome*, *6*. doi: 10.1186/s40168-018
1064 -0401-z
- 1065 Bentley, D. R., Balasubramanian, S., Swerdlow, H. P., Smith, G. P., Milton, J.,
1066 Brown, C. G., ... Smith, A. J. (2008). Accurate whole human genome
1067 sequencing using reversible terminator chemistry. *Nature*, *456*(7218), 53–
1068 59. doi: 10.1038/nature07517
- 1069 Boore, J. L. (1999). Animal mitochondrial genomes. *Nucleic Acids Research*,
1070 *27*(8), 1767–1780. doi: 10.1093/nar/27.8.1767
- 1071 Cameron, S. L. (2014). Insect mitochondrial genomics: Implications for evolution
1072 and phylogeny. *Annual Review of Entomology*, *59*, 95–117. doi: 10.1146/
1073 annurev-ento-011613-162007
- 1074 Dierckxsens, N., Mardulyn, P., & Smits, G. (2017). Novoplasty: de novo assembly
1075 of organelle genomes from whole genome data. *Nucleic Acids Research*,

- 1076 45(4), e18. doi: 10.1093/nar/gkw955
- 1077 Edgar, R. C. (n.d.). *Uchime in practice*. Retrieved from https://www.drive5.com/usearch/manual7/uchime_practical.html
- 1079 Edgar, R. C. (2016). Uchime2: improved chimera prediction for amplicon sequencing. *bioRxiv*. Retrieved from <https://api.semanticscholar.org/CorpusID:88955007>
- 1082 Edgar, R. C., Haas, B. J., Clemente, J. C., Quince, C., & Knight, R. (2011).
1083 Uchime improves sensitivity and speed of chimera detection. *Bioinformatics*,
1084 27(16), 2194–2200. doi: 10.1093/bioinformatics/btr381
- 1085 Glenn, T. C. (2011). Field guide to next-generation dna sequencers. *Molecular
1086 Ecology Resources*, 11(5), 759–769. doi: 10.1111/j.1755-0998.2011.03024.x
- 1087 Gonzalez, J. M., Zimmermann, J., & Saiz-Jimenez, C. (2004, 09). Evaluating
1088 putative chimeric sequences from pcr-amplified products. *Bioinformatics*,
1089 21(3), 333-337. Retrieved from <https://doi.org/10.1093/bioinformatics/bti008> doi: 10.1093/bioinformatics/bti008
- 1091 Gray, M. W. (2012). Mitochondrial evolution. *Cold Spring Harbor perspectives
in biology*, 4. Retrieved from <https://doi.org/10.1101/cshperspect.a011403> doi: 10.1101/cshperspect.a011403
- 1094 Hahn, C., Bachmann, L., & Chevreux, B. (2013). Reconstructing mitochondrial
1095 genomes directly from genomic next-generation sequencing reads—a baiting
1096 and iterative mapping approach. *Nucleic Acids Research*, 41(13), e129. doi:
1097 10.1093/nar/gkt371
- 1098 Jin, J.-J., Yu, W.-B., Yang, J., Song, Y., dePamphilis, C. W., Yi, T.-S., & Li,
1099 D.-Z. (2020). Getorganelle: a fast and versatile toolkit for accurate de
1100 novo assembly of organelle genomes. *Genome Biology*, 21(1), 241. doi:
1101 10.1186/s13059-020-02154-5

- 1102 Judo, M. S. B., Wedel, W. R., & Wilson, B. H. (1998). Stimulation and sup-
1103 pression of pcr-mediated recombination. *Nucleic Acids Research*, 26(7),
1104 1819–1825. doi: 10.1093/nar/26.7.1819
- 1105 Labrador, K., Agmata, A., Palermo, J. D., Ravago-Gotanco, R., & Pante, M. J.
1106 (2021). Mitochondrial dna reveals genetically structured haplogroups of
1107 bali sardinella (sardinella lemuru) in philippine waters. *Regional Studies in*
1108 *Marine Science*, 41, 101588. doi: 10.1016/j.rsma.2020.101588
- 1109 Li, H. (2018, 05). Minimap2: pairwise alignment for nucleotide sequences. *Bioin-*
1110 *formatics*, 34(18), 3094-3100. Retrieved from <https://doi.org/10.1093/bioinformatics/bty191>
1111 doi: 10.1093/bioinformatics/bty191
- 1112 Liang, Q., Bible, P. W., Liu, Y., Zou, B., & Wei, L. (2020, 02). Deepmi-
1113 crobes: taxonomic classification for metagenomics with deep learning. *NAR*
1114 *Genomics and Bioinformatics*, 2(1), lqaa009. Retrieved from <https://doi.org/10.1093/nargab/lqaa009> doi: 10.1093/nargab/lqaa009
- 1116 Metzker, M. L. (2010). Sequencing technologies — the next generation. *Nature*
1117 *Reviews Genetics*, 11(1), 31–46. doi: 10.1038/nrg2626
- 1118 Mysara, M., Saeys, Y., Leys, N., Raes, J., & Monsieurs, P. (2015). Catch,
1119 an ensemble classifier for chimera detection in 16s rrna sequencing stud-
1120 ies. *Applied and Environmental Microbiology*, 81(5), 1573-1584. Retrieved
1121 from <https://journals.asm.org/doi/abs/10.1128/aem.02896-14> doi:
1122 10.1128/AEM.02896-14
- 1123 Peccoud, J., Lequime, S., Moltini-Conclois, I., Giraud, I., Lambrechts, L., &
1124 Gilbert, C. (2018, 04). A survey of virus recombination uncovers canon-
1125 ical features of artificial chimeras generated during deep sequencing li-
1126 brary preparation. *G3 Genes—Genomes—Genetics*, 8(4), 1129-1138. Re-
1127 trieved from <https://doi.org/10.1534/g3.117.300468> doi: 10.1534/

- 1128 g3.117.300468
- 1129 Qin, Y., Wu, L., Zhang, Q., Wen, C., Nostrand, J. D. V., Ning, D., ... Zhou, J.
1130 (2023). Effects of error, chimera, bias, and gc content on the accuracy of
1131 amplicon sequencing. *mSystems*, 8(6), e01025-23. Retrieved from <https://journals.asm.org/doi/abs/10.1128/msystems.01025-23> doi: 10.1128/
1132 msystems.01025-23
- 1133
- 1134 Qiu, X., Wu, L., Huang, H., McDonel, P. E., Palumbo, A. V., Tiedje, J. M., &
1135 Zhou, J. (2001). Evaluation of pcr-generated chimeras, mutations, and het-
1136 eroduplexes with 16s rrna gene-based cloning. *Applied and Environmental*
1137 *Microbiology*, 67(2), 880–887. doi: 10.1128/AEM.67.2.880-887.2001
- 1138 Ren, J., Song, K., Deng, C., Ahlgren, N., Fuhrman, J., Li, Y., ... Sun, F. (2020,
1139 01). Identifying viruses from metagenomic data using deep learning. *Quan-*
1140 *titative Biology*, 8. doi: 10.1007/s40484-019-0187-4
- 1141 Rodriguez-Martin, B., Palumbo, E., Marco-Sola, S., Griebel, T., Ribeca, P.,
1142 Alonso, G., ... Djebali, S. (2017, 01). Chimpipe: Accurate detection of
1143 fusion genes and transcription-induced chimeras from rna-seq data. *BMC*
1144 *Genomics*, 18. doi: 10.1186/s12864-016-3404-9
- 1145 Rognes, T., Flouri, T., Nichols, B., Quince, C., & Mahé, F. (2016). Vsearch: a
1146 versatile open source tool for metagenomics. *PeerJ*, 4, e2584. doi: 10.7717/
1147 peerj.2584
- 1148 Sedlazeck, F., Rescheneder, P., Smolka, M., Fang, H., Nattestad, M., von Haeseler,
1149 A., & Schatz, M. (2018, 06). Accurate detection of complex structural
1150 variations using single-molecule sequencing. *Nature Methods*, 15. doi: 10
1151 .1038/s41592-018-0001-7
- 1152 Sfeir, A., & Symington, L. S. (2015). Microhomology-mediated end joining: A
1153 back-up survival mechanism or dedicated pathway? *Trends in Biochemical*

- 1154 *Sciences*, 40(11), 701-714. Retrieved from <https://www.sciencedirect.com/science/article/pii/S0968000415001589> doi: <https://doi.org/10.1016/j.tibs.2015.08.006>
- 1155
- 1156
- 1157 Vervier, K., Mahé, P., Tournoud, M., Veyrieras, J.-B., & Vert, J.-P. (2015,
1158 11). Large-scale machine learning for metagenomics sequence classifica-
1159 tion. *Bioinformatics*, 32(7), 1023-1032. Retrieved from <https://doi.org/10.1093/bioinformatics/btv683> doi: 10.1093/bioinformatics/btv683
- 1160
- 1161 Willette, D., Bognot, E., Mutia, M. T., & Santos, M. (2011). *Biology and ecology
1162 of sardines in the philippines: A review* (Vol. 13; Tech. Rep. No. 1). NFRDI
1163 Technical Paper Series. Retrieved from <https://nfrdi.da.gov.ph/tpjf/etc/Willette%20et%20al.%20Sardines%20Review.pdf>
- 1164